PROCEEDINGS OF SCIENCE

Neutron stars: The journey from birth to death.

Jirina R Stone[a,*]

[a] *University of Oxford,*
Department of Physics (Astro), University of Oxford, Keble Rd, OX1 3RH Oxford, United Kingdom

E-mail: jirina.stone@physics.ox.ac.uk

This paper contains the synopsis of my three lectures given at the XV International Workshop on Hadron Physics.The first lecture covers introduction to the general life cycle of stars and the origin of compact objects, followed by the history of neutron stars discovery and their macroscopic features together with a survey of the latest astrophysical observation techniques. The second lecture is devoted to macroscopic and microscopic nuclear physics models of the equation of state governing the cold neutron stars. A special attention is paid to the Quark-Meson-Coupling model, an effective relativistic mean-field model in which the forces between individual baryons are self-consistently mediated by exchange of virtual mesons between the valence quarks in the baryons. In the third lecture (i) similarities and differences between dense matter created in heavy ion collisions and the cores of neutron stars, (ii) gravitational waves from binary neutron star merges and (iii) the impact of data in the multimessenger era on deeper understanding of neutron star interiors are discussed.

XV International Workshop on Hadron Physics (XV Hadron Physics) 13 -17 September 2021
Online, hosted by Instituto Tecnológico de Aeronáutica, São José dos Campos, Brazil

*Speaker

PoS(XVHadronPhysics)002

Contents

1. Introduction

In the first lecture, I first introduce the general life cycle of stars and the origin of compact objects, followed by the history of neutron stars (NSs) discovery and their general macroscopic features, together with the survey the latest astrophysical observation techniques.

The second lecture is devoted to exploration of the NS Equation of State (EoS) which is still unknown and is a subject of extensive research. Among the variety of theoretical and empirical models of the EoS currently in the literature, I describe in more detail the Quark-Meson-Coupling (QMC) model, an effective relativistic mean-field model in which the forces between individual

baryons are self-consistently mediated by exchange of virtual mesons between the valence quarks in the baryons.

The neutron star merger (BNSM) and the related gravitational waves (GW) are the subject of the final, third lecture. This topic is currently most actively explored, using novel frameworks of multi-messenger techniques. Advantages and disadvantages of this trend will be discussed.

These lectures are based on my recent paper [1] where interested reader may find more details of the material presented here.

2. Lecture I: General features of compact objects from observation

In this lecture we discuss the history of NSs discovery, their general macroscopic features together with the survey the latest astrophysical observation techniques.

2.1 Life cycle of stars and the origin of compact objects

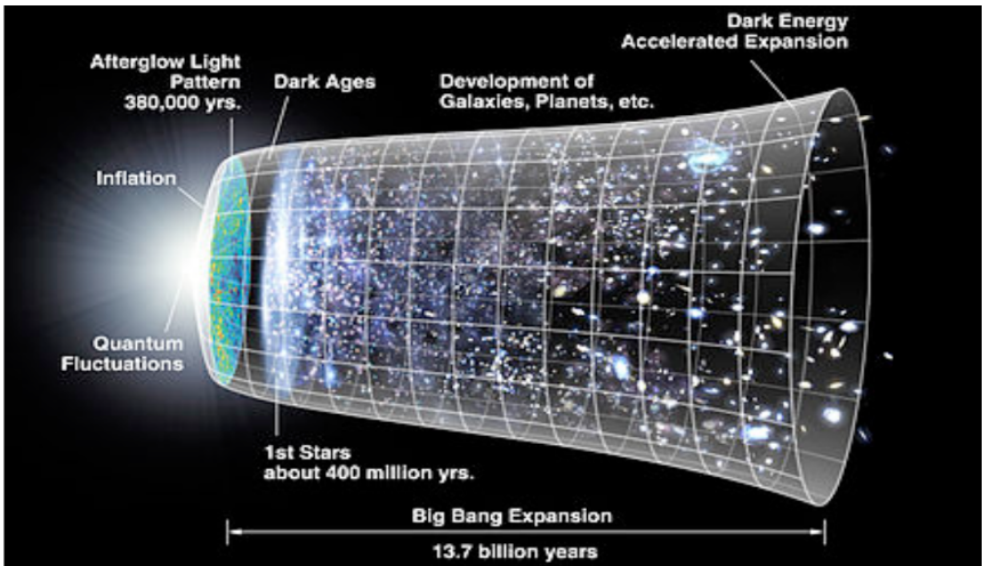

Figure 1: Evolution of the observable part of our Universe from the Big Bang (left) to the present (right). Taken from Wikimedia Commons, the free media repository.

The history of evolution of our Universe, as we understand it at present, is illustrated in Fig. 1. The current hypothesis is that first stars developed from stellar clouds and their life cycle is governed by their gravitational mass. Over 90% of stars in our Galaxy are of low or medium mass below 8 $M_\odot$ (main-sequence stars).

Stars with mass lower than the Chandrasekhar limit of 1.4 $M_\odot$ evolve through the sequence illustrated in the top row of Fig. 2:

- Hydrogen (H) fusing into helium (He) and and the star expands to a red giant;
- Helium fusing to carbon (C) and oxygen (O) in the core by the triple alpha process;

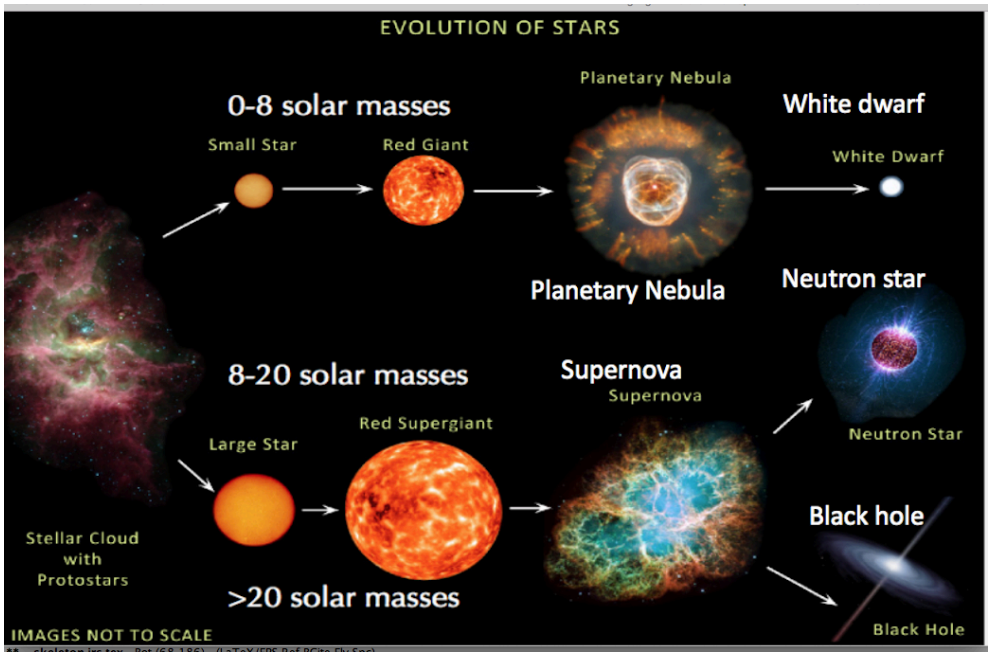

Figure 2: Evolution of stars in dependence of their gravitational mass. The figure has been adopted by courtesy of Andrew Steiner.

– If the temperature is too low to fuse carbon, C and O accumulate in the core and the outer envelope sheds off to form planetary nebula, returning the light elements back to interstellar medium and a white dwarf is born.

White dwarfs are supported against gravitational collapse by electron degeneracy pressure may have a different composition in dependence on their mass and temperature, such as (CO), (ONeMg), (ONe), (He) and different fate. For example, if a CO white dwarf mass exceeds 1.4 $M_\odot$ it may expode as type 1a supernova (carbon detonation).

Stars heavier than about 1.4 $M_\odot$ proceed beyond the white dwarf stage and the gravitational collapse continues until the nuclear density is reached and the nucleon degeneracy pressure starts to hold the collapse. At this stage nuclear reactions are proceeding with cross sections enhanced by the star increasing temperature. High-energy gamma-rays cause the endothermic photodisintegration of nuclei into alpha particles, which decreases the kinetic energy of the electrons in the core, further lowers the pressure and speeds up the collapse. The rate of electron capture on protons is enhanced with increasing density and temperature, leading to neutronization of the matter and to production of neutrinos. The decrease of the electron fraction contributes to further lowering of the pressure. Neutrinos escape from the star core as their mean free path is much larger than the initial radius of the core. They remove energy from the core and deplete the number of all leptons thus further decreasing the core pressure.

When the collapse reaches the stage that nuclei start to touch, the core matter is transformed into a nearly degenerate, highly incompressible Fermi gas of nucleons. At some density above the saturation density (~ 0.16 fm$^{-}3$) the core rebounces, forming a shock wave of material to the outer

Table 1: Examples of supernova remnants observed in the Milky way and some nearby Galaxies. The constellations in which they appear, apparent magnitude, distance in light years, host galaxies and the associated pulsars (when observed) are given. Spectroscopic classification is explained in Fig. 3. Type IIb is transitional between Type II (i.e. with H lines) to Type Ib (i.e., dominated by He lines). Ipec and IIpec stand for peculiar, meaning that these supernovae may have different progenitors than red giants and are still under study. For definition of apparent magnitude see https://en.wikipedia.org/wiki/Apparent_magnitude.

Remnant	Type	Constellation	App. Mag.	Dist.(lY).	Host Galaxy	Pulsar
Vela 11000	II	Vela	+12.0	815±98	NGC 2736+	PSR J0835
SN 1054 (Crab)	II	Taurus	-6	6,500	Milky Way	PSR B0531+21
SN CasA 1680	IIb	Cassiopeia	+5	11,000	Milky Way	CXOU J232327.8+584842
SN 1885A	Ipec	Andromeda	+7	2,500,000	M31	–
SN 1987A	IIpec	Dorado	+2.9	160,000	Lar.Mag.Cloud	See Ref. [3]
SN 2008D	Ibc	Lynx		88,000,000	NGC 2770	–

space in a core-collapse supernova (CCSN - Type II) event. If the core mass is less than about 20 $M_{\odot}$, it forms a proto-neutron star (middle row in Fig. 2), otherwise the core collapse continues, eventually becoming a black hole (bottom row in Fig. 2) Some examples of the most studied CCSN

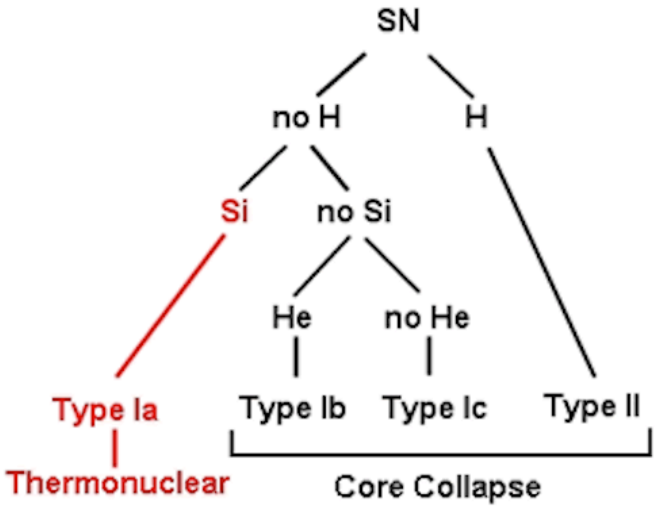

Figure 3: Supernova classification tree. Adopted from https://astronomy.swin.edu.au/cosmos/S/Supernova+Classification.

events are listed in Table 1. Analysis of electromagnetic signals, mostly radio and X-rays, reveal information about dynamics and chemical composition of the remnants. In particular, the latter is employed to learn about the status of the progenitor stars and to classify the remnants as illustrated in Fig. 3. An interesting example of supernova observation is shown in Fig. 4, the only time when a supernova event was detected in action by Soderberg et al. [2].

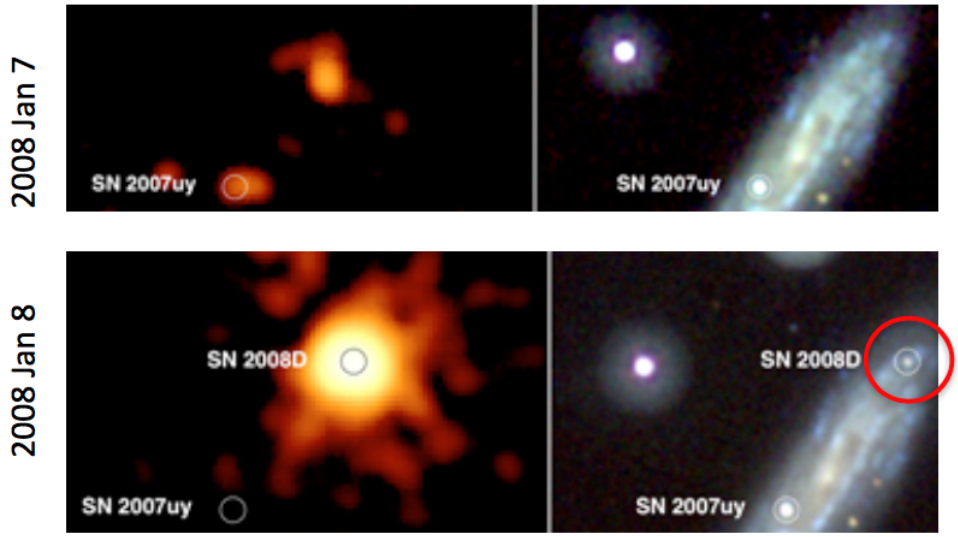

Figure 4: Image of the SN 2008D from the NASA Swift X-ray telescope. Top: galaxy NGC 2770 with SNR 2007uy before SN 2008D. Bottom: The same but after SN 2008D. Left (right) panels show X-ray (visible light) images.

2.2 Discovery of neutron stars

Although supernova remnants have been observed for a long time, the origin of neutrons stars as a consequence of a supernova event was identified much later. Baade (1898-1974) and Zwicky (1893-1960) coined a special class of novae (new stars) with extraordinary brightness super-novae for the first time in Proc. Nat. Astr. Soc. Communicated in March 19, 1934 (announced 15-16 December 1933). Based on analysis of data on the remnant of SN 1885A, they suggested generation of a compact object in the process. In their publication [4] they identified this object with a NS with the comment *We are fully aware that our suggestion carries with it grave implications regarding the ordinary views about the constitution of stars and therefore will require further careful studies*. In the 1930's, a NS was envisaged as an object made of about 10^{57} uniformly distributed neutrons within a sphere with radius of about 10 km and mass 1.5 $M_{\odot}$. It is remarkable that the current notion of the complex interior of a NS (see Fig. 5) is not very far from these early estimates. However, direct observation of NSs has been difficult. They do not have a source of energy after formation and use only energy inherited from the CCSN process. In addition, they have a small surface, their initial cooling is rapid within (fraction of) seconds and their optical luminosity is low.

A new era in exploration of compact objects started with the discovery of pulsars in 1967 by Jocelyn Bell Brunell and Anthony Hewish as a source of pulsed radio emission from outside of the solar system (PSR J1921+2153 in the constellation of Velpecula 'The fox') and later identification of pulsars with highly magnetized NSs. Much later pulsars were recognized as sources of powering the nebulae formed in CCSN events, with the Crab pulsar, discovered in 1968, being the first.

With fast development of observational techniques, electromagnetic signals from pulsars were found across a wide range of wavelengths. For example, the emission from the Crab nebula was originally observed in X-ray and visible light spectra (see Fig. 6) but more recently high-energy

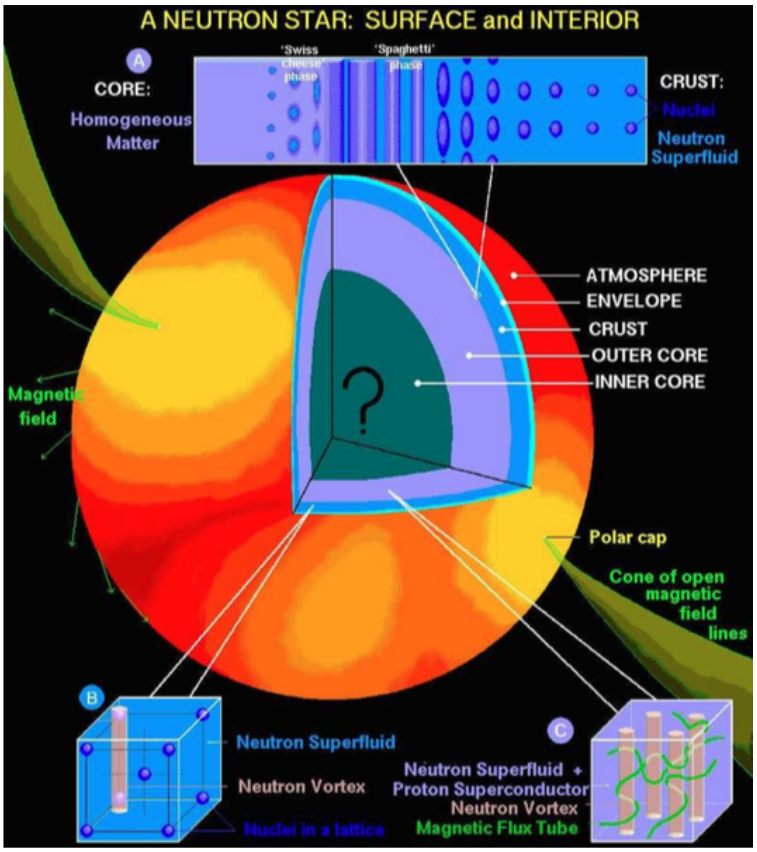

Figure 5: Cartoon of interior structure of a cold neutron star. Courtesy of Dany Page, taken from research-gate.net.

gamma rays were also detected [5], making it the first known source of ultra-high-energy cosmic rays.

The origin of pulsed emission of radiation has been usually ascribed to fast rotation of a highly magnetized object with the uniform dipole magnetic field. The tilt between the rotation and magnetic axes makes the pulsar behave as the cosmic lighthouse with the beam of radiation sweeping around the space (see Fig. 7). It is assumed that the rotating magnetic star induces a strong electric quadrupole field in its surroundings. This field pulls charges from the star surface forming a dense plasma, the magnetosphere, which is forced by the magnetic field to co-rotate with the star. The magnetosphere can extend only to a distance where the co-rotating velocity reaches the speed of light. This distance defines the light cylinder which separates the magnetic field lines into closed and open. The plasma inside the cylinder remains trapped but the plasma on the open field lines can leave the magnetosphere and create a beam of particles, or electromagnetic waves, at a distance tens to hundred km above the pulsar surface [6]. If the beam sweeps over the Earth, it is perceived as being pulsed.

Observations show that the pulsar periods is increasing, i.e. the rotation is slowing down. Investigation of isolated pulsars (not in a binary) suggests that the mechanism of this change in rotation period is far from understood. The measure of changes of the rotation period, the braking

Figure 6: A composite image of the Crab nebula. The X-ray image (blue) and the optical image (red) are superimpost. The pulsar is the red star in the center. Adopted from Chandra-crab.jpg, taken from Wikimedia Commons, the free media repository. The size of the X-ray image is smaller because the higher energy X-ray emitting electrons radiate away their energy more quickly than the lower energy optically emitting electrons as they move. Source: https://hubblesite.org/contents/media/images/2002/24/1248-Image.html. Authors:Optical: NASA/HST/ASU/J, Hester et al. X-Ray: NASA/CXC/ASU/J, Hester et al.

index, is not in agreement with a simple magnetic dipole radiation [9]. It is likely affected by a more complicated structure of the pulsar magnetic field [10]. This research is still in progress.

2.3 Properties of NSs from observation

Observation of NSs provides two vital pieces of data, the gravitation mass and radius. As discussed later, these two quantities are not independent. The reason is that the Tolman-Oppenheimer-Volkoff (TOV) equation, which constraints the mass and radius of a spherically symmetric body of isotropic material using general relativity (GR) and governs the NS physics, provides the gravitational mass of the body only as a function of its radius (see Sect. 3.1). While several reliable methods have been developed for measurement of gravitational mass of NSs, independent determination of both quantities on one object was reported only very recently (see below), with a rather large error on the radius [11]. It is important to note that NS mass can be measured only in binary systems in which at least one component is a pulsar (but only 5-10% of known pulsars are in binaries).

In any binary system, there exist five orbital parameters (Keplerian parameters), which can be precisely measured. The eccentricity of the orbit, the orbital period, the projection of the

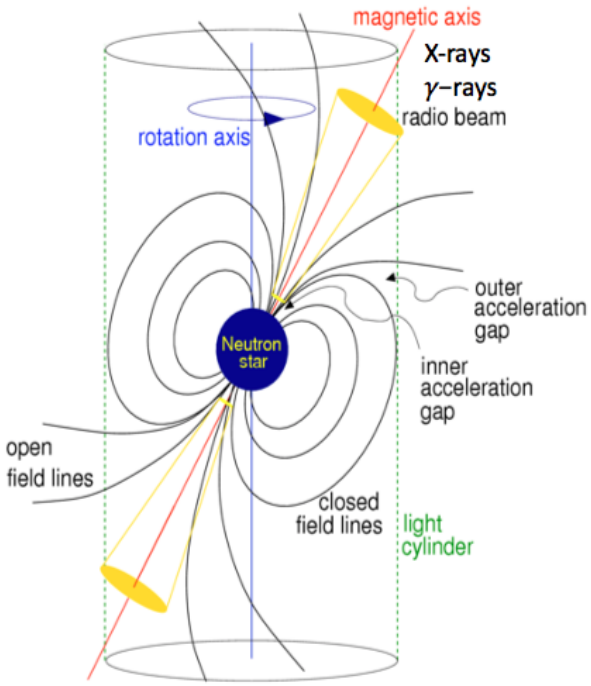

Figure 7: Schematic mechanism of a pulsar. Adopted from Refs. [6–8].

pulsar's semi-major axis on the line of sight and the time and longitude of the periastron. These parameters can be related to the masses of the NS and its companion through a mass function f [12]. Deviations from the Keplerian orbit due to GR effects are parametrized in terms of one or more post-Keplerian parameters. The most significant ones include the advance of the periastron of the orbit, the combined effect of variations in the transverse Doppler shift and gravitational redshift around an elliptical orbit, the orbital decay due to the emission of quadrupole gravitational radiation, and the range and shape parameters that characterize the Shapiro time delay of the pulsar signal as it propagates through the gravitational field of its companion. The post-Keplerian parameters can be written in terms of measured quantities and the masses of the star and its companion [13]. Measurement of any two of these post-Keplerian parameters together with the mass function f is sufficient to determine uniquely the masses of the two components of the system [12].

The first binary system discovered was the Hulse-Taylor PSR B1913+16 pulsar, P=59 ms, whose periodic changes in radio pulse frequency led to discovery of an unknown NS companion. The mass of the pulsar, M_g = 1.4414±0.0002 $M_\odot$ ($M_\odot$ being the solar mass) is the most precisely known NS mass to date, leading to adoption of this mass as 'canonical'. However, both lighter and heavier NS were observed later, such as, for example,

– PSR J0737-3039 the first double pulsar (A,B); P = 2.77s (B) M_g = 1.249±0.001 $M_\odot$ (Lyne et al. 2004, [14]);

– PSR J1903+0327 NS on an eccentric orbit around MS star; P = 59 ms M_g=1.667±0.021 $M_\odot$ (Freire et al. 2011 [15]);

- PSR J1614-2230 NS+WD P = 3.15 ms M_g = 1.97±0.04 $M_\odot$ (Demorest et al. 2010 [16]), 1.928 ± 0.017 $M_\odot$ (Fonseca et al. 2016 [17]), 1.908 ± 0.016 $M_\odot$ (Arzoumanian et al. 2018 [18]);
- PSR J0348+0432 NS+WD P = 39 ms M_g = 2.03±0.03 $M_\odot$ (Antoniadis et al. 2013 [19]);
- PSR J0740+6620 NS+WD P=2.89 ms M_g = 2.14±0.10 $M_\odot$ (Cromartie et al. 2019 [20]), M_g = 2.08±0.07 $M_\odot$ (Fonseca et al. 2021 [21]).

We refer the reader to a very useful up-to-date list of pulsar masses and their relation to testing GR at https://www3.mpifr-bonn.mpg.de/staff/pfreire/NS_masses.html.

Determination of NS radii is complicated by our limited knowledge distance, atmosphere, disk area, medium composition between the star and the observer and some estimate of the NS mass (usually taken as 1.4 $M_\odot$).

One of the most frequent source of data for NS radii are low mass X-ray binaries. The X-rays are produced by matter falling from one component, (normal star), to the other component, a neutron star or a black hole. When the in-falling material reaches the surface of the NS and the ignition temperature is high enough, an X-ray burst appears, which forms raw data for estimation the NS radius.

Table 2: Selected methods and results of measuring NS radii. For mor details see text.

Authors	Method	Radius
Steiner et al. 2013 [22]	X-ray	10.4 - 12.9 km
Ozel and Freire 2016 [23]	X-ray	10 – 11.5 km
Annala et al. 2018 [24]	GW	13.6 km
Abbott et al. 2018 [25]	GW	11.9 ± 1.4 km
Burgio et al. 2019 [26]	GW+elmg	11.8 – 13.1 km (for 1.5 $M_\odot$)
Capano et al. 2020 [27]	GW	10.4 - 11.9 km
Al-Mamun et al. 2021 [28]	GW+elmg	9.8 – 13.95 km

With the advent of GW generated in merger of compact objects, several methods of extracting NS radius have been developed (see more detail in Section 4.2). The detected pre-merger GW signal (no post-merger data exist yet) is analysed assuming properties of the objects, namely their gravitational masses and their EoSs, thus making the procedure model dependent. The main idea has been to use constraints on the tidal effects of the coalescing objects, and translate them to constraints on their radii. The usual assumption is that the mass of the cold, non-rotating objects is around 1.4 $M_\odot$ (either equal or unequal) and their EoS, as well as description of dynamics merger process vary [24, 25]. Multi-messenger approaches to inference of NS radii include the electromagnetic counterparts, the kilonova AT2017gfo signal [26] and also the gamma-ray burst [27] to the analysis. Ultimately, data from observation of quiescent low-mass X-ray binaries (QLMXBs), photospheric radius expansion X-ray bursting sources, and X-ray timing observations of PSR J0030+0451 were reported to have been included in the simulation. Illustrative example of such analysis has been

reported in a recent paper [28] and is illustrated in Fig. 8. The limit on the radius of the 1.4 $M_\odot$ NS is shown in Fig. 8. Miller et al. [11] obtained, for the first time, the equatorial circumferential

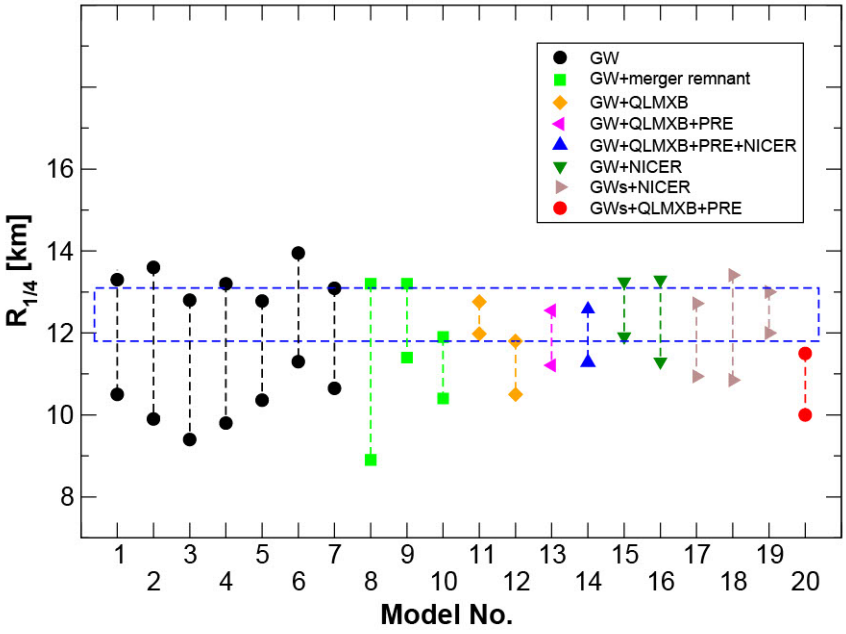

Figure 8: Radius of a NS with a fixed gravitational mass 1.4 $M_\odot$ as extracted from data on GW170817 alone, combined GW170817 and GW190425 events, and GW data in combination with electromagnetic data from NICER, quiescent low mass X-ray binaries (QLMXB), and photo-spheric radius expansion X-ray burst source (PRE) observations. The figure has been adopted from Ref. [1] (under the Creative Commons Attribution License) where the references to individual models and other details can be found. The models are labeled by numbers: (1) [25], (2) [24], (3) [29], (4) [30], (5,15) [31], (6,7,13,14) [28], (8) [32], (9) [33], (10) [27], (11) [34], (12) [35], (16) [36], (17) [37], (18) [38, 39], (19,20) [40]. The results of individual models are presented with the 90% credibility level except for models 6,7,13 and 14 quoting 95% credibility. The dashed blue box shows the constraint on the radius reported by [11].

radius of PSR J0740+6620 (heaviest pulsar known at present) with the known mass using NICER and XMM-Newton Data (see below) to be $13.7^{+2.6}_{-1.5}$ km with 68% credibility. A combination of this result with a previous NICER mass and radius measurement of PSR J0030+0451, the masses of two other ~ 2 $M_\odot$, and the tidal deformability constraints from two GW events was used in a three different frameworks of the EoS modelling. The results were consistent in a density range from 1.5 to 5 times nuclear saturation density and yielded full radii 12.45±0.65 km for a 1.4 $M_\odot$ NS and 12.35±0.75 km for a 2.08 $M_\odot$ neutron star. It is broadly compatible with many other results using similar methods (some referenced in the caption of Fig. 8), although it indicates preference for larger radii as indicated with the blue dashed rectangle. It is obvious that the field is not there yet and it may be that a precision of more than a few percent is needed to make impact on theory of NS.

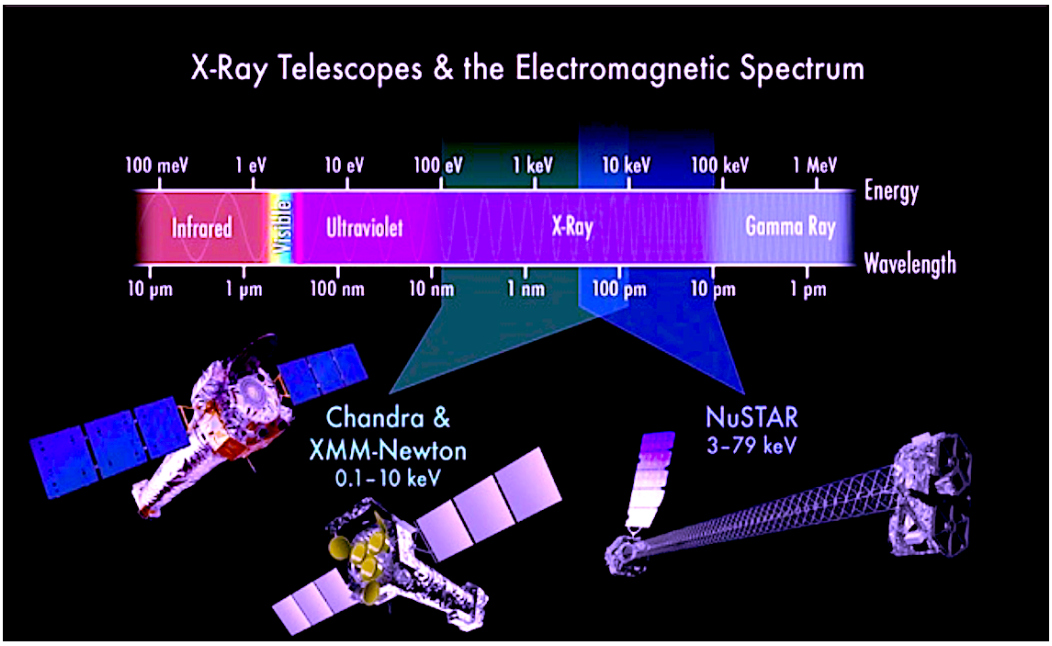

Figure 9: X-ray telescopes and the electromagnetic spectrum sensitivity of XMM Newton, NuSTAR and Chandra. Courtesy of NASA.

Despite a lot of effort in this field, the currently extracted radii using different (combination of) methods, including GW, span a rather wide range from about 10 to 14 km. Examples of some results are given in Table 2.

2.4 Observational techniques

At the end of this lecture we wish to make a note about space observatories which are currently used to study properties of compact objects (see Fig. 9):

- XMM Newton (X-ray Multi-Mirror Mission-Space telescope) was launched by European Space Agency in 1999 and is still in orbit. It studied for the first time the influence of the gravitational field of a pulsar on the light it emits. It is sensitive to X-rays from compact objects atmospheres and mapped the growth of $\sim$ 12,000 supermassive black holes in the cores of galaxies and galaxy clusters;

- NuSTAR (Nuclear Spectroscopic Telescope Array), launched by NASA in 2012, has deployed the first orbiting telescopes to focus light in the high energy X-ray (3-79 keV). It consists of two co-aligned grazing incidence telescopes with specially coated optics and newly developed X-ray detectors;

- Chandra X-ray observatory, named by Subrahmanyan Chandrasekhar, launched by NASA in 1999 as being about 100 times more sensitive to X-rays than any previous X-ray telescope, due to the high angular resolution of its mirrors. Chandra is an Earth satellite in a 64-hour orbit, and its mission is ongoing as of 2022. It is NASA flagship mission of X-ray astronomy.

It provided the first light image of the remnant SN CasA, showed the never-before-seen ring around the central pulsar in the Crab nebula and the first data on X-ray emission from the supermassive hole in the center of the Milky Way, among other valuable data, such as the first observation of an exoplanet outside the Milky Way.

The two most recent X-ray telescopes, NICER (Neutron Star Interior Composition Explorer) and IXPE (Imaging X-ray Polarization Explorer) represent a significant improvement in technology, promising data never accessible before.

NICER was launched by NASA in 2017 and placed at the International Space Station. The novelty of NICER is that it provides simultaneous fast timing and spectroscopy data with a high signal to noise ratio within 0.2-12 keV X-ray band (has 56 X-ray concentrator optics and silicon drift detector pairs). Timing-based techniques rely on the presence of surface inhomogeneities (hot spots, see https://www.sciencedaily.com/releases/2018/04/180404093938.htm) and [41]), leading to photon emission that varies periodically as the star rotates [42].

IXPE is designed to study X-ray production in NS and pulsar wind nebulae, as well as stellar and supermassive black holes. It is different from all the other X-ray telescopes that it detects polarization of the X-rays, i.e. the angle of rotation of a plane of polarized light which complements the data already available. The energy range of sensitivity is 2-8 keV. It was launched in December 2021 by NASA and first data are expected to operate for about 2 years.

Finally we mention the two most famous telescopes which are sensitive to low-energy electromagnetic signals, the Hubble and James Webb space telescope (JWST). The Hubble observes in the near ultraviolet, visible, and near infrared (wavelength 0.1–1.0 μm) range, and JWST is sensitive to light with wavelength 0.6–28.3 μm (orange to mid-infrared). The objective of these telescopes is to look as far as possible in space towards the early Universe. JWST will detect objects up to 100 times fainter than Hubble, and objects back to redshift z≈20 (about 180 million years cosmic time after the Big Bang). For comparison, the earliest stars are thought to have formed between z≈30 and z≈20 (100-180 million years cosmic time) and the first galaxies may have formed around redshift z≈15 (about 270 million years cosmic time). Hubble has not been able to see further back than the very early reionization at z≈11.1 (Galaxy GN-z11, 400 million years cosmic time) (see https://en.wikipedia.org/wiki/James_Webb_Space_Telescope and refs. therein).

3. Lecture II: Neutron star interior and the Equation of State

The second lecture is devoted to exploration of the NS EoS, which is still unknown and Is a subject of extensive research. Among the variety of theoretical and empirical models of the EoS currently in the literature, we describe in more detail the Quark-Meson-Coupling (QMC) Model, an effective relativistic mean-field model in which the forces between individual baryons are self-consistently mediated by exchange of virtual mesons between the valence quarks in the baryons.

We start with the 'big' picture, the QCD diagram of high density matter in a 3D space of temperature and chemical potentials: baryon μ_B=3/2(μ_u + μ_d) and isospin μ_I=1/2(μ_u − μ_d) with u and d stand for up and down quarks, respectively. The somewhat unusual representation of the diagram is useful because it includes the location of NS (blue area), supernovae and NS mergers

(red area), as well as the region accessible to heavy-ion collisions (grey lines), as illustrated in Fig. 10. The diagram also marks the area of pion condensates, the hadron-quark phase transition and different phases of quark matter.

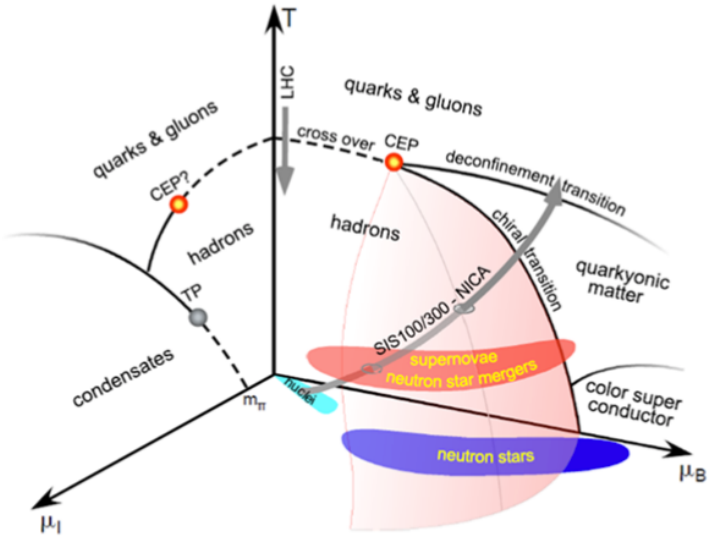

Figure 10: QCD diagram of high density matter. Taken from the NuPECC Long Range Plan 2017 'Perspectives for Nuclear Physics' https://www.esf.org/fileadmin/user_upload/esf/Nupecc-LRP2017.pdf. For more explanation see also Refs. [43, 44].

Extracting the expected composition of high density matter in NS from the general diagram, i.e. for low T and high μ_B, we find a wealth of species possibly present in NS cores, as demonstrated in Fig. 11. Addressing all the features shown in this picture it goes beyond the scope of this lecture. We concentrate only on the fermion hadronic sector of the core, leaving the quark matter and it phases and the boson condensates for another occasion.

3.1 The Equation of State

The key property of high-density matter with uniform baryon number density ρ is the EoS, the relation between pressure P, total energy density ε, and temperature T. In analogy with the ideal gas, we write

$$P = \varepsilon(\rho, T) \qquad \varepsilon(\rho, T) = \sum_f \left(\frac{E}{A}(\rho, T)\rho\right)_f \qquad \mu_B = (P + \varepsilon)/\rho \tag{1}$$

where E/A stands for energy per particle of a fraction f in the matter. There are two key points to make:

- The EoS is dependent on composition of the matter (summing over f);
- The energy per particle E/A of each component and its density and temperature dependence must be determined by nuclear and particle models.

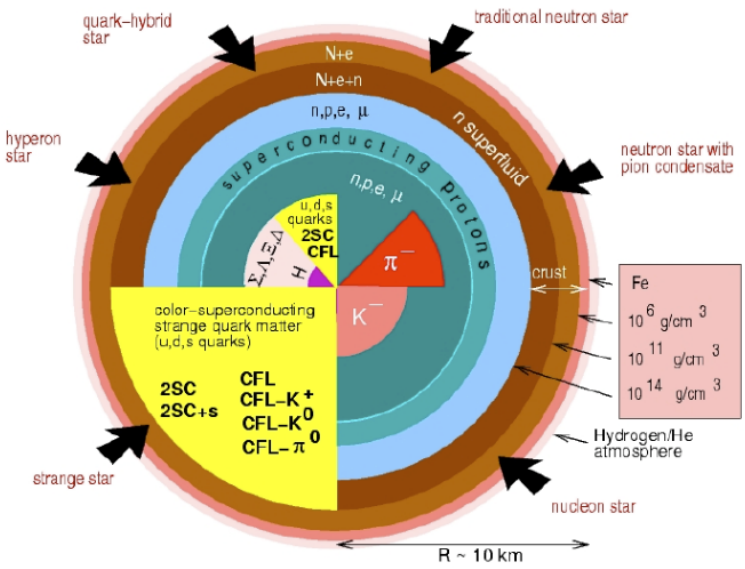

Figure 11: Cold neutron star interior as modelled by Weber et al. [45].

The EoS rules the macroscopic properties of NS. It forms input to the general relativistic Tolman-Oppenheimer-Volkoff (TOV) equation for hydrostatic equilibrium of a spherical object with isotropic mass distribution. The equation yields gravitational mass of the object as a function of its radius. The TOV equation reads

$$\frac{dP}{dr} = -\frac{GM(r)\varepsilon}{r^2}\frac{(1+P/\varepsilon c^2)(1+4\pi r^3 P/M(r)c^2)}{1-2GM(r)/rc^2} \qquad (2)$$
$$M(r) = \int_0^r 4\pi r'^2 \varepsilon(r'^2) dr'^2,$$

with P and ε are input at each particle number density ρ (note that $P = \rho(\partial\varepsilon/\partial\rho) - \varepsilon$ where $\partial\varepsilon/\partial\rho$ is the chemical potential μ). The result is illustrated in Fig. 12, showing the relation between the EoS and the output from the TOV equation. Each point on the M(R) curve corresponds to one NS model with a given P and ε in the EoS. Models on the left from the maximum mass are not stable (for explanation see [46]).

There are two difficulties with the TOV solutions. First, the solution does not provide mass and radius of a NS separately which is a fundamental problem. As discussed on Section 2, obtaining both mass and radius of the same object has been achieved only very recently on one star with a large uncertainty. The NICER mission has been designed to avoid this problem but it still faces the second issue, the dependence on the EoS. There are many variants of microscopic and phenomenological models of hadronic matter in the literature with various levels of complexity. In addition, a choice of components of hadronic matter in different model vary from nucleon-only to the full baryon octet and baryon resonances (p, n, Λ, Σ, Ξ, Δ), and mesons (pions, kaons, delta and H-dibaryon condensates). A selection of mass radius curves, calculated using different EoS of NS with the simplest cores containing only nucleons and lepton (electrons and muons) is shown in Fig. 13. With the particle composition fixed, the various shapes reflect only the differences in nuclear models.

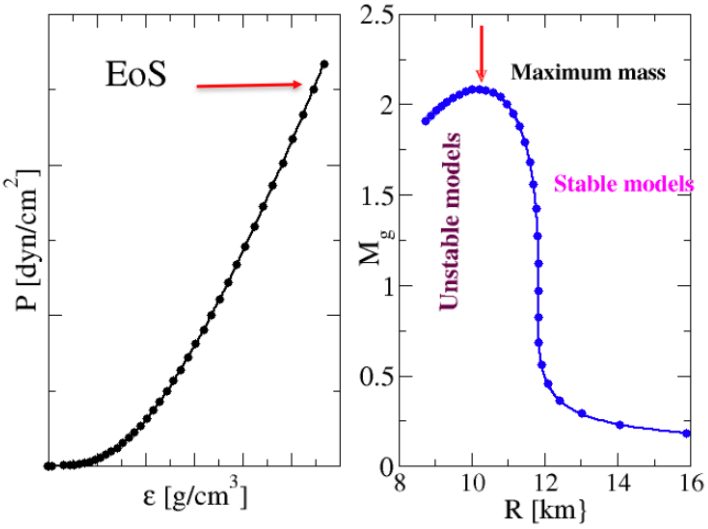

Figure 12: Correspondence between the solution of the TOV equation and the EoS. For more explanation see text.

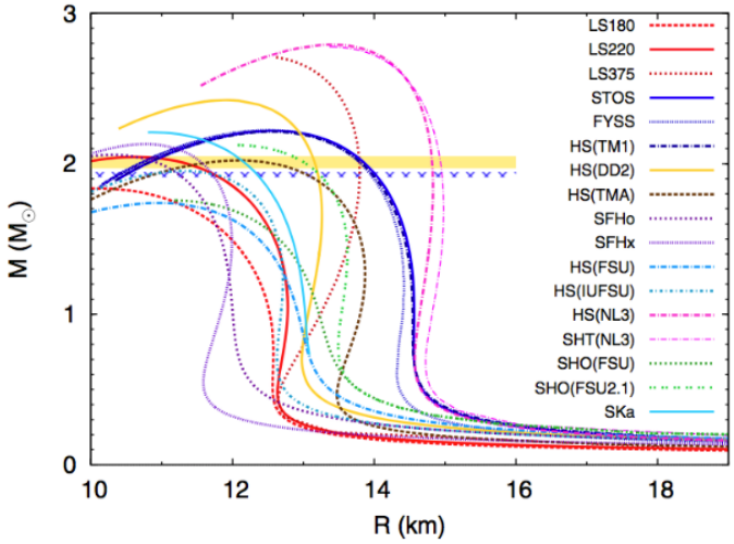

Figure 13: Selection of M-R curves of cold NSs containing only n, p, e and μ in the core. Adopted from Ref. [47].

3.2 Nuclear physics input to the EoS

The main problem of all models in nuclear physics is that fundamental properties of the forces, acting between baryons in free space and their modification by nuclear medium are unknown. The latter is usually referred to as *the nuclear many-body problem* which is most challenging for all computational techniques in use today. We will outline only a few major classes of models of high density matter, based on different principles and, not surprisingly, yielding different results. The

focus will be on the way these models predict the energy per particle E/A of individual components as a function of baryon number density, to obtain the total energy density of the system which is then processed to determine NS properties.

3.2.1 Macroscopic phenomenological models

The most successful phenomenological model of the nucleus is based on the more than 80 years old semi-empirical mass formula (SMF), developed in 1935 by von Weizsacker [48] and elaborated in 1936 by Bethe and Bacher [49]. The nucleus was modelled as a spherical drop of incompressible liquid. The binding energy of a nucleus with A=N+Z nucleons and the binding energy per particle E/A is expressed as

$$B(A,Z) = a_{\rm vol}A + a_{\rm surf}A^{2/3} + a_{\rm C}Z^2A^{-1/3} + a_{\rm sym}(N-Z)^2A^{-1} \quad (3)$$

$$E/A \equiv B(A,Z)/A = a_{\rm vol} + a_{\rm surf}A^{-1/3} + a_{\rm C}Z^2A^{-4/3} + a_{\rm sym}(N-Z)^2A^{-2}, \quad (4)$$

where $a_{\rm vol}$, $a_{\rm surf}$, $a_{\rm C}$ and $a_{\rm sym}$ are coefficients of the volume, surface, Coulomb and symmetry terms. These coefficient are determined by fitting the binding energy to experimental nuclear masses, $M(A,Z) = (Zm(^1H) + Nm_{\rm n} - B(A,Z))/c^2$.

The mass number independence of the volume term in Eq. 4 led to introducing the concept of infinite nuclear matter (INM) ([49, 50] and refs. therein), a hypothetical medium made up of infinite number of uniformly distributed protons and neutrons, with a given proton/neutron ratio, and no Coulomb force. INM has only two properties that can be calculated, the binding energy per particle and the particle number density.

The binding energy per particle of INM with N = Z, the symmetric nuclear matter (SNM), E_0/A, is given by the coefficient $a_{\rm v}$ in Eq. 4 because all the other terms tend to zero for A $\rightarrow \infty$ and N = Z. To calculate the particle number density of the SNM ρ_0, an assumption has to be made concerning nuclear radius. The standard expression for the mass number dependence of nuclear radius $R = r_0A^{1/3}$ is used with the constant r_0 must be determined for experiment (more discussion can be found in [1].

The constancy of the E_0/A and ρ_0 in SNM has a fundamental meaning. The constant density implies that there must be a balance between attractive and repulsive components of the nuclear force which are equilibrated at that density - *the saturation density*. The number of surrounding nucleons for each nucleon at saturation density must the same, independent of its position in space. Assuming the nuclear force is of a short range, comparable with the inter-nucleon distance, each nucleon will interact only with a few nucleons around it, resulting, on average, in the same contribution to the total binding energy per particle, i.e. *the saturation energy*. The current most frequently adopted values of ρ_0 and E_0/A are 0.16 fm^{-3} and -16 MeV, respectively. These values are fundamental calibration points for most of the low energy nuclear structure models.

Interest in calculation of nuclear masses led to development of the SMF to a series of liquid drop models, which included more realistic features of atomic nuclei, such as arbitrary shapes, surface diffuseness and shell corrections (see e.g. [51] and refs. therein). These models are purely phenomenological and do not require knowledge of the nuclear force. A microscopic part in a form of a schematic nuclear potential [52] was added later, to construct a microscopic-macroscopic model, extensively used in calculation of nuclear masses at present.

To study other bulk nuclear properties in nuclei and nuclear matter, different strategies for parameterizations of the energy per particle were used, based on Taylor expansion around the SNM values. In addition, other forms of nuclear matter were introduced, the asymmetric matter with N≠Z (ANM) and pure neutron matter (PNM) with Z=0. The symmetry energy S, being approximately equal to the difference between E/A in SNM and PNM at ρ_0, its first derivative (slope) L and the second derivative K (incompressibility) were defined.

There has been a consolidated effort to find experimental and theoretical constraints for the S, L and K parameters and their density dependence without a general consensus being reached. Analysis of relevant experiments is model dependent in most cases, and the data themselves often suffer from large uncertainties (see e.g. [53–56]). The value of S is reasonably well constrained between about 28 - 34 MeV, but the current (model dependent) limit on the range of L at ρ_0 remains between about 30 - 100 MeV, and its density dependence is not constrained. The incompressibility K ranges between low values, around 220 - 240 MeV in non-relativistic models, mainly based on experiments with giant resonances and Skyrme-type models), and above ~ 260 MeV in relativistic models of high density matter [57, 58].

3.2.2 Microscopic "realistic" models based on free-space NN interactions

The main idea of these models is to extract nucleon-nucleon (NN) potentials from scattering experiments in free space and to include the medium effect by mathematical techniques into calculation of the total energy density (and derived quantities) of a system. The potentials typically depend on 10-40 parameters perfectly fitted data on NN-scattering phase shifts and properties of the deuteron. For example, soft-core Reid, non-relativistic family of Argonne and relativistic families of Nijmegen and Bonn potentials have been frequently used.

There are two problems with this method. First, the bare NN interactions are not density dependent and are not additive in many-body systems as, for example, the Coulomb interaction. Second, all the potentials are phase-shift equivalent i.e. various forms of the NN interaction are fitted to the same data set; it follows that it is not possible to single out the one which is closest to reality.

Many methods have been developed to reproduce properties of the SNM, such as Brueckner–Hartree–Fock (BHF), Dirac–Brueckner–Hartree–Fock (DBHF), variational chain summation, V_{lowk}, Fermi hypernetted chain/single-operator chain, Quantum Monte Carlo and auxiliary-field diffusion Monte Carlo (AFDMC) formalism, as well other methods, including limitation of high momentum components in the scattering amplitudes and renormalization schemes (see e.g. [59] for a review). We show in Fig. 14 predictions for density dependence of E/A by 20 realistic NN potentials (for details see [60] and refs. therein). The black curves represent potentials which provide too strong binding on the BHF level. Including three-body forces (TBF) (Paris, V14, and V18; red curves) adds considerable repulsion and yields results less repulsive than the DBHF ones with the Bonn potentials (green curves). It is obvious the reproducing the saturation properties of SNM is quite a challenge for these types of models.

Another system modelled with realistic potentials is PNM. Such system does not exit in nature but all theories suggest that PNM is not bound, i.e. E/A is always positive. There has been a lively activity in this field, exploring sub-saturation region of particle number density up to about $3 \times \rho_0$ [61–64]. The uncertainty in the density dependence of E/A in PNM is illustrated in Figs. 15 and

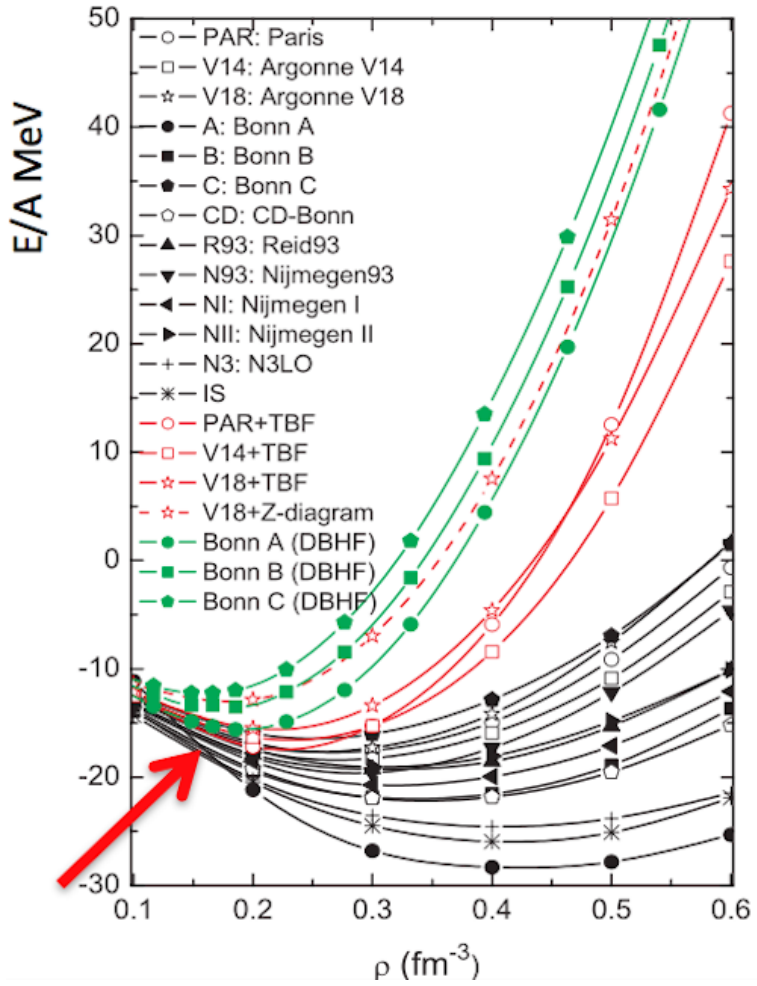

Figure 14: Density dependence of the energy per particle E/A in SNM as predicted by realistic models. Adopted from Ref. [60]. The red arrow marks the SNM saturation point.

16. In Fig. 15 the E/A is obtained using the AV8′ NN interaction alone (lower symbols and line) and with the UIX 3N force. In Fig. 16 the top and bottom lines are the same as in Fig. 15 but using various models for the 3N (three-neutron) force, computed for different values of the symmetry energy (note that E_{sym} in the figure is S in our notation). The band around each value of E_{sym} shows the effect of different spatial and spin structures of the 3N interaction. Note that the spread in values of E/A at about 3 ρ_0 between the models is more than a factor of two, although at about ρ_0 is very small. Again, selection of a preferred model is not possible.

3.2.3 Chiral effective field theory

A popular tool providing interactions for modeling high density matter *up to about twice nuclear saturation density* is the chiral effective field theory χEFT, proposed in 1990's by Weinberg [65, 66]. The χEFT model has been formulated in terms of nucleons, their excitations, and pions, instead of quarks and gluons e.g.[67]. It provides a systematic low momentum expansion of long- and

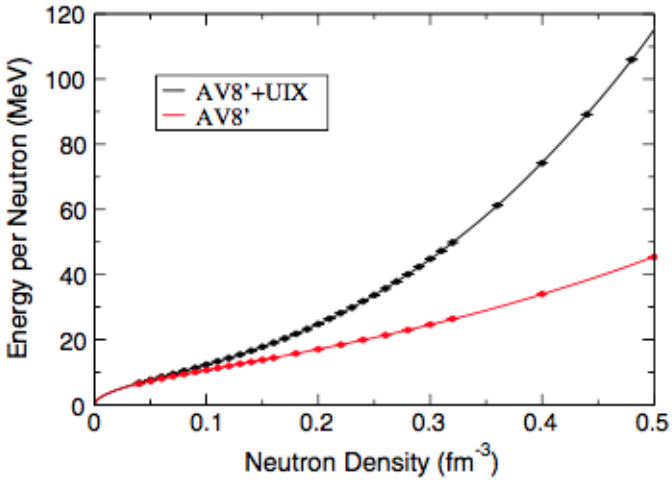

Figure 15: Density dependence of the energy per particle E/A in PNM, obtained using the Argonne AV8′ NN interaction alone (lower symbols and line) and with the UIX 3N force. Taken from Ref. [63].

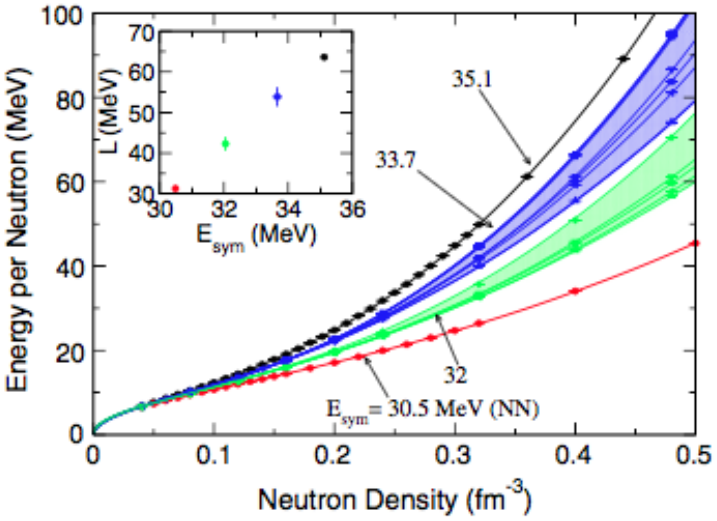

Figure 16: The same as Fig. 15 but for various 3N forces computed for different values of the nuclear symmetry energy ($E_{sym} \equiv S$). For each value of E_{sym} the corresponding band shows the effect of different spatial and spin structures of the 3N interaction. The inset shows the linear correlation between E_{sym} and its density derivative, the slope, L. Taken from Ref. [63].

medium-range forces between nucleons and pions, consistent with the spontaneously broken QCD chiral symmetry. The short-range forces are parameterized by contact terms (solid symbols in the diagrams in Fig. 17) constrained by parity, time-reversal and the usual conservation laws, but not by chiral symmetry. These terms have to be fitted to experiment. The χEFT expansions have to be regulated by a cut-off parameters, eliminating high momentum components, which must

be determined by comparison with data. The χEFT provides a systematic hierarchy of nuclear interactions by including the three-body and higher order forces naturally on the same footing. This is a positive aspect of the χEFT theory which, however, remains phenomenological and does not offer a unique solution to the many-body problem.

There has been an increasing number of applications of NN forces derived from χEFT (for reviews see [68–70]). We illustrate in Fig. 17 a schematic diagram of the hierarchy of chiral nuclear forces up to N4LO (next-to-next-to-next-to-next-leading order). Not all the diagrams have been worked out yet and some questions regarding convergence of the series are still being investigated.

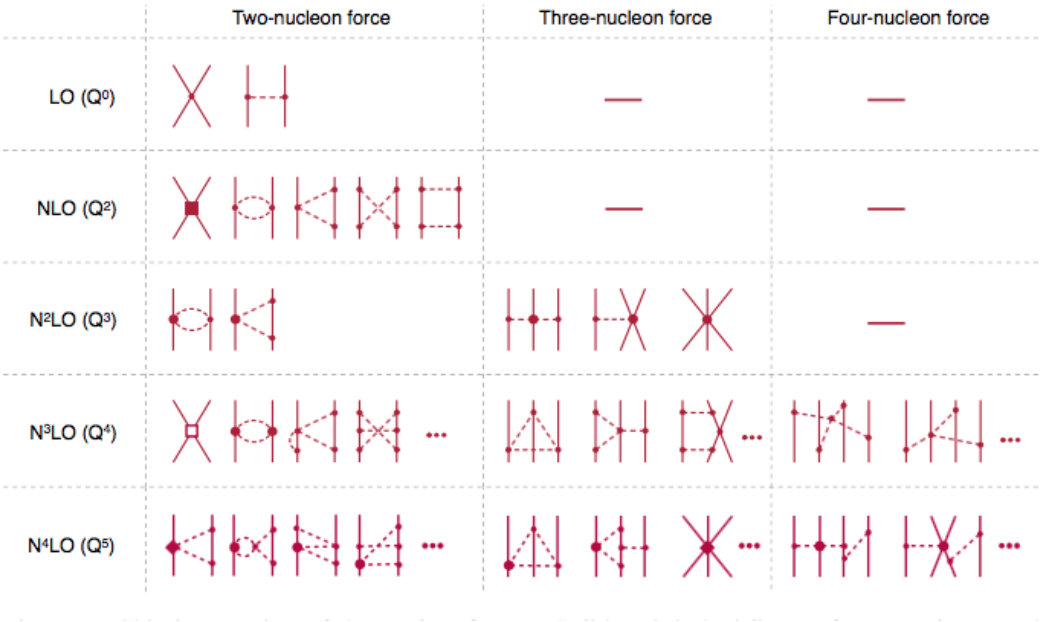

Figure 17: Chiral expansion of the nuclear forces. Solid and dashed lines are for nucleons and pions, respectively. Solid dots, filled circles, rectangles, diamonds and open rectangles illustrate vertices of dimension $\Delta_i = 0$, $\Delta_i = 1$, $\Delta_i = 2$, $\Delta_i = 3$ and $\Delta_i = 4$, respectively. Taken from Ref. [71] where more details are given.

Illustration of performance of χEFT interactions to predict binding energies per particle of selected light oxygen, calcium and nickel even-even nuclei is shown Fig. 18. Chiral EMN potentials [72] at NLO, N2LO and N3LO orders, with the three-body interaction at N2LO and N3LO level, fitted to saturation properties of SNM and the binding energy of the triton, have been used [73]. We observe that on the whole the nuclei are over-bound at the NLO level and converge to under-binding with the increasing orders. The final total binding energy still differs from experiment by several tens of MeV. The radii (not shown here) are systematically too large.

Typical EoS of PNM and SNM calculated with EMN chiral potentials are shown in the right panel (b) of Fig. 18 [74] (right). Although the error bands are reduced in N3LO as compared to N2LO, they diverge significantly above the saturation density. The main challenge is to extend these models to higher densities relevant to interior of neutron stars which is currently outside their capability.

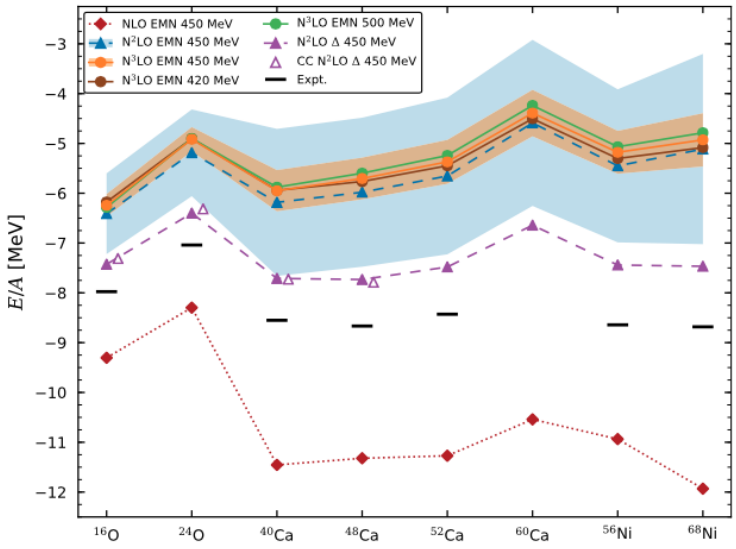

Figure 18: Ground state binding energy per particle of oxygen, calcium and nickel closed-(sub)shell even-even nuclei calculated with EMN potentials at the N3LO order and cutoffs Λ= 420, 450, and 500 MeV indicated by the brown, orange, and green-solid lines and circles, respectively. Experimental data are shown as short horizontal black bars. The results for the N2LO (NLO) order are marked with a dashed (dotted) line. The figure was taken from Ref. [73].

3.2.4 Mean-field models with density-dependent effective NN interactions

Another approach to computation of properties of nuclear matter is to parameterize the density dependence of the effective NN force directly. This approach is less fundamental but has a number of advantages. The calculation is simpler, offering a better insight into properties of the force. It offers a satisfactory description of binding energies, radii and level densities not only of stable nuclei but also far from stability and superdeformed nuclei. The main disadvantage however, is the necessity of introducing about 10-15 correlated parameters. These parameters are not well constrained and, in principle, allow construction of an infinite number of a funcional form of the force.

3.2.4.1 Non-relativistic Skyrme model We demonstrate the problem using one of the most-popular non-relativistic density dependent forces, the Skyrme force [75–77]. The full Hamiltonian, applicable for nuclear matter and finite nuclei reads [78]

$$H = T + H_0 + H_3 + H_{eff} + H_{fin} + H_{so} + H_{sg}, \tag{5}$$

where individual terms stand for the kinetic energy, the zero range (H_0), three-body equivalent density dependent term (H_3) and the effective mass part (H_{eff}). These terms are not dependent on derivatives of density (left column of the expressions below) and are used to calculate properties of nuclear matter. The last three terms are needed for modelling of finite nuclei (right hand expressions) are a finite range term (H_{fin}), the spin-orbit term (H_{so}) and a term due to the tensor coupling with spin and gradient (H_{sg}) . We included the Coulomb and pairing terms in the H_{sg} for brevity.

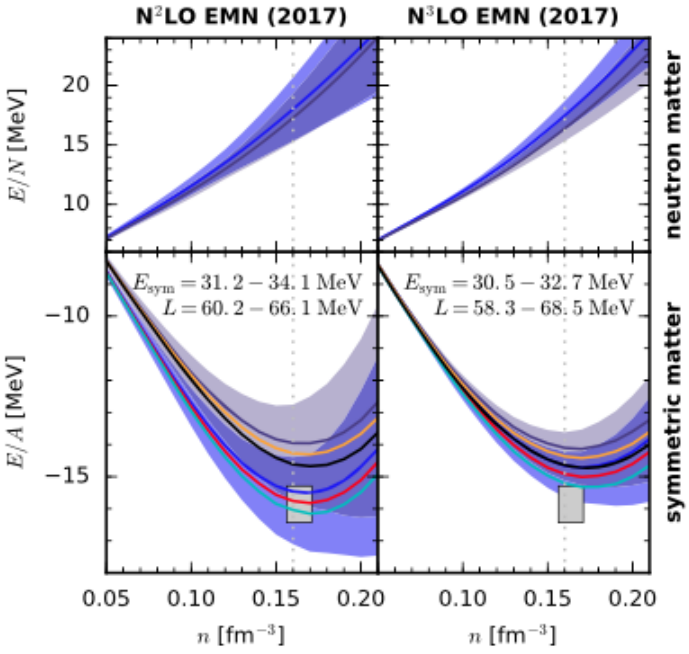

Figure 19: Energy per particle E/A as a function of particle number density n calculated in N2LO (left panel) and N3LO (right panels). The shaded areas represent theoretical uncertainties. The rectangles indicate ranges of the empirical values of the saturation density and energy of SNM. The vertical dotted line is drawn at ρ_0=0.16 fm^{-3}. The figure was adapted from Ref. [74]. The ranges of the symmetry energy $S \equiv E_{sym}$ and its slope L are displayed in the bottom panels. For more details see the original reference.

$$H_o = \tfrac{1}{4}t_0\left[(2+x_0)\rho^2 - (2x_0+1)(\rho_p^2+\rho_n^2)\right]$$
$$H_3 = \tfrac{1}{24}t_3\rho^\alpha\left[(2+x_3)\rho^2 - (2x_3+1)(\rho_p^2+\rho_n^2)\right]$$
$$H_{eff} = \tfrac{1}{8}\left[t_1(2+x_1)+t_2(2+x_2)\right]\tau\rho + \tfrac{1}{8}\left[t_2(2x_2+1)-t_1(2x_1+1)\right]\left(\tau_p\rho_p+\tau_n\rho_n\right)$$
$$H_{fin} = \frac{1}{32}\left[3t_1(2+x_1)-t_2(2+x_2)\right](\nabla\rho)^2 - \frac{1}{32}\left[3t_1(2x_1+1)-t_2(2x_2+1)\right]\left[(\nabla\rho_p)^2+(\nabla\rho_n)^2\right]$$
$$H_{so} = \frac{1}{2}W_0\left[J.\nabla\rho + J_p.\nabla\rho_p + J_n.\nabla\rho_n\right]$$
$$H_{sg} = -\frac{1}{16}(t_1x_1+t_2x_2)J^2 + \frac{1}{16}(t_1-t_2)\left[J_p^2+J_n^2\right] + H_{coul} + H_{pair}$$

The symbols in red, t_0, t_1,t_2,t_3 and x_0,x_1,x_2,x_3 are adjustable parameters. Dutra et al. [54] collected 240 sets of the Skyrme force parameters of the nuclear matter part of the Hamiltonian (left column), reported in the literature in 2012 and tested their performance in predicting an extensive set experimental constraints on a variety of nuclear matter and neutron star properties. They discovered that only 5 set satisfied all the constraints. It was not possible to justify success of these 5 on a physical basis. These sets had nothing in common and were fitted to data in different model frameworks.

3.2.4.2 Relativistic mean-field models Relativistic mean-field models (RMF) have been widely used as they have of several important features not always present in nonrelativistic models. Intrinsic Lorentz covariance, spin-orbit interaction, saturation mechanism in nuclear matter and causality

are automatically included (for a recent review see [79]). RMF models are based on the notion that baryons interact by exchange of σ, ω, ρ and δ mesons. The most general Lagrangian density for hadronic matter in the RMF most frequently used variant, non-linear Walecka model, reads [79]

$$\mathcal{L}_{\rm NL} = \mathcal{L}_{\rm nm} + \mathcal{L}_{\sigma} + \mathcal{L}_{\omega} + \mathcal{L}_{\rho} + \mathcal{L}_{\delta} + \mathcal{L}_{\sigma\omega\rho}$$

$$\begin{aligned}
\mathcal{L}_{\rm nm} &= \overline{\psi}(i\gamma^{\mu}\partial_{\mu} - M)\psi + g_{\sigma}\sigma\overline{\psi}\psi - g_{\omega}\overline{\psi}\gamma^{\mu}\omega_{\mu}\psi \\
&\quad - \frac{g_{\rho}}{2}\overline{\psi}\gamma^{\mu}\vec{\rho}_{\mu}\vec{\tau}\psi + g_{\delta}\overline{\psi}\vec{\delta}\vec{\tau}\psi, \\
\mathcal{L}_{\sigma} &= \frac{1}{2}\left(\partial^{\mu}\sigma\,\partial_{\mu}\sigma - m_{\sigma}^{2}\sigma^{2}\right) - \frac{A}{3}\sigma^{3} - \frac{B}{4}\sigma^{4}, \\
\mathcal{L}_{\omega} &= -\frac{1}{4}F^{\mu\nu}F_{\mu\nu} + \frac{1}{2}m_{\omega}^{2}\omega_{\mu}\omega^{\mu} + \frac{C}{4}\left(g_{\omega}^{2}\omega_{\mu}\omega^{\mu}\right)^{2}, \\
\mathcal{L}_{\rho} &= -\frac{1}{4}\vec{B}^{\mu\nu}\vec{B}_{\mu\nu} + \frac{1}{2}m_{\rho}^{2}\vec{\rho}_{\mu}\vec{\rho}^{\mu}, \\
\mathcal{L}_{\delta} &= \frac{1}{2}\left(\partial^{\mu}\vec{\delta}\partial_{\mu}\vec{\delta} - m_{\delta}^{2}\vec{\delta}^{2}\right),
\end{aligned}$$

$$\begin{aligned}
\mathcal{L}_{\sigma\omega\rho} &= g_{\sigma}g_{\omega}^{2}\sigma\omega_{\mu}\omega^{\mu}\left(\alpha_{1} + \tfrac{1}{2}\alpha_{1}'g_{\sigma}\sigma\right) \\
&\quad + g_{\sigma}g_{\rho}^{2}\sigma\vec{\rho}_{\mu}\vec{\rho}^{\mu}\left(\alpha_{2} + \tfrac{1}{2}\alpha_{2}'g_{\sigma}\sigma\right) \\
&\quad + \tfrac{1}{2}\alpha_{3}'g_{\omega}^{2}g_{\rho}^{2}\omega_{\mu}\omega^{\mu}\vec{\rho}_{\mu}\vec{\rho}^{\mu}.
\end{aligned}$$

where $\mathcal{L}_{nm}$ stands for the kinetic part of the nucleons plus interactions between them and the σ, ω, ρ and δ mesons. The $\mathcal{L}_i$ represent the free and self-interacting terms of the σ, ω, ρ and δ mesons. The last term, $\mathcal{L}_{\sigma\omega\rho}$, accounts for cross interactions between the meson fields. Looking at the general Lagrangian $\mathcal{L}_{NL}$, the $\mathcal{L}_{nm}$ depends only on four coupling constants g, but the other terms bring in another seven parameters, making the total of eleven, of the same order as the Skyrme model. In addition, there are many variants of RMF models in the literature. Dutra et al. [55] in 2014 examined 263 variants of the model and confronted them with two sets of bulk nuclear matter properties, one more and one less restrictive. As a result, only 4 models satisfying the constraints were identified.

3.2.4.3 Quark-Meson-Coupling Model The Quark-Meson-Coupling model was developed by Guichon and collaborators [80–83] as a special class of relativistic mean field models. The fundamental difference between the traditional RMF and the QMC models is that in the QMC model the forces between individual baryons are *self-consistently* mediated by exchange of virtual σ, ω and ρ meson fields between the valence quarks in the baryons (see Fig. 20). The effect of the medium surrounding the baryons in dense matter, such as in NS cores and nuclei, modifies dynamics of the valence quarks in the individual baryons. In other words, *in the nuclear medium the quark-meson couplings acquire an effective density dependence which is determined by the response of the quark structure of the baryons to the meson fields*.

The total energy of a *classical* system of baryons, modeled as non-overlapping bags coupled to meson fields σ, ω and ρ is expressed as [83]

$$E_{QMC} = \sum_{i=1,\ldots} \sqrt{P_i^2 + M_i^2(\sigma(\vec{R}_i))} + g_{\omega}^{i}\omega(\vec{R}_i) + g_{\rho}\vec{I}_i.\vec{B}(\vec{R}_i) + E_{\sigma} + E_{\omega,\rho}, \tag{6}$$

with $\vec{R}_i$ and $\vec{P}_i$ being the position and momentum of a baryon i and $\vec{I}$ is the isospin matrix. E_{σ} and $E_{\omega,\rho}$ are static meson fields energies. Following the notation of Ref. [83], $\vec{B}$ stands here for the isovector ρ field to avoid a confusion with the baryon number density ρ [83].

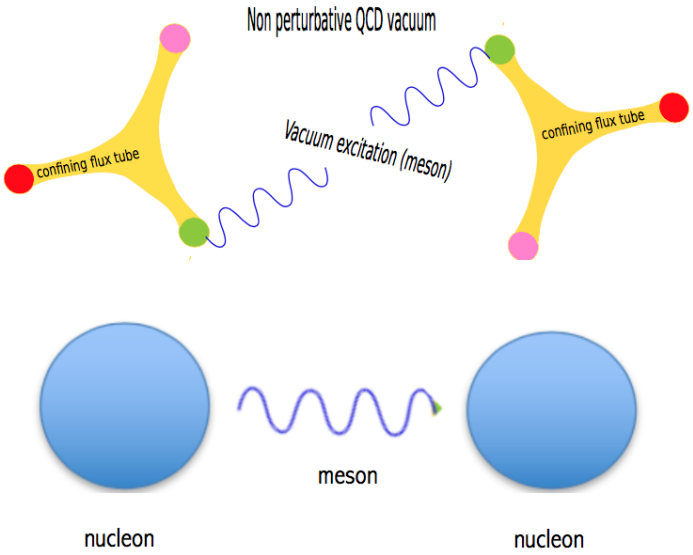

Figure 20: Cartoon of the mechanism of interaction in the QMC model. Shown is the distribution of valence quarks and gluon tubes as predicted by Lattice QCD (see http://www.physics.adelaide.edu.au/theory/staff/leinweber/VisualQCD/Nobel/index.html) (top). The figure has been adapted from Ref. [83]. Traditional image of interaction between baryons without considering their internal structure (bottom).

The dynamical mass of a bag, representing a baryon i (short for b(i)) immersed in a constant scalar field is obtained by solving the bag equations to be

$$M_i(\sigma) = M_i - w_{\sigma i}\, g_{\sigma N}\, \sigma + \frac{d}{2}\tilde{w}_{\sigma i}(g_{\sigma N}\, \sigma)^2. \tag{7}$$

The quark-meson couplings are related to the nucleon couplings to σ, ω and ρ mesons in free space as

$$g_{\sigma N} = 3g^q_\sigma \int_{Bag} d\vec{r}\, \bar{q}q(\vec{r}) \qquad g_{\omega N} = 3g^q_\omega \qquad g_{\rho N} = g^q_\rho, \tag{8}$$

where q is the valence quark wave function for a free bag.

The effective coupling constants G_σ, G_ω, and G_ρ are introduced for convenience

$$G_\sigma = \frac{g^2_{\sigma N}}{m^2_\sigma} \qquad G_\omega = \frac{g^2_{\omega N}}{m^2_\omega} \qquad G_\rho = \frac{g^2_{\rho N}}{m^2_\rho}, \tag{9}$$

using the free σ, ω and ρ meson masses.

The coefficient d in the third term in Equation 7 is known as the "scalar polarizability" and is a fundamental feature of QMC. It is a natural consequence of the quark structure of the nucleon and is sufficient to lead to nuclear saturation. The scalar polarizability is related to the radius of the bag R_B as [83]

$$d = 0.0044 + 0.211R_B - 0.0357R^2_B. \tag{10}$$

.

The weights $w_{\sigma i}$ and $\tilde{w}_{\sigma i}$ control the flavor dependence of the effective mass and in a naive first approximation they are equal to 1+s(i)/3 (s being strangeness), since the σ meson is taken to couple only to the non-strange light quarks. This simple relation is however broken by the difference in bag radii of the hyperons as well as the hyperfine color interaction. The exact values are also dependent on the bag radii and the experimental masses of the nucleon, Δ, and Λ, Σ and Ξ hyperons. R_B is constrained by the nucleon radius in free space and the weights summarized in Table 2 [83] (see also the Appendix in the Ref. [84]).

The meson fields are time independent and can be eliminated through the equations of motion

$$\frac{\delta E_{QMC}}{\delta\sigma(\vec{r})} = \frac{\delta E_{QMC}}{\delta\omega(\vec{r})} = \frac{\delta E_{QMC}}{\delta B_\alpha(\vec{r})} = 0\,. \tag{11}$$

Equation 6 is then quantized by replacement

$$\vec{P}_i \rightarrow -i\vec{\nabla}_i. \tag{12}$$

The heavy σ, ω and ρ mesons account for the exchange of correlated pions, but single pion exchange must be added separately, however this does not involve any additional parameters. The full Hamiltonian reads (for details see [83])

$$H_{QMC} = H_\sigma + H_\omega + H_\rho + H_{so} + H_\pi. \tag{13}$$

For practical use, we use expansion of the mean field σ assuming that the field operator σ can be written as

$$\sigma = \langle\sigma\rangle + \delta\sigma, \tag{14}$$

where the *C-number* $\langle\sigma\rangle \equiv \bar{\sigma}$ denotes the ground state expectation value and the fluctuation $\delta\sigma$ is considered as a small quantity (the term C number is a nomenclature used by Paul Dirac which refers to real and complex numbers. It is used to distinguish from operators [q-numbers or quantum numbers] in quantum mechanics). Using this expansion, the σ part of the Hamiltonian becomes $\langle H_{QMC}\rangle$ and the full Hamiltonian reads [83]

$$\langle H_{QMC}\rangle = \langle H_\sigma\rangle + \langle H_\omega\rangle + \langle H_\rho\rangle + \langle H_{so}\rangle + \langle H_\pi\rangle. \tag{15}$$

This Hamiltonian significantly simplifies in infinite nuclear matter, a medium with uniform density ρ without surface and spin-orbit effects. All gradient terms vanish and $\langle H_{QMC}\rangle$ reduces to $\langle H_{NM}\rangle$. The ground state of the system is specified by a set of Fermi levels and the σ exchange part of the expression for the total energy density is calculated in the Hartree-Fock approximation [84]. The ω and ρ exchange can be calculated exactly as they are purely 2-body. Finally the long-range pion exchange is added and we write

$$\varepsilon = \frac{\langle H_\sigma\rangle}{V} + \frac{\langle V_\omega\rangle}{V} + \frac{\langle V_\rho\rangle}{V} + \frac{\langle V_\pi\rangle}{V}. \tag{16}$$

The energy per particle is then calculated as

$$E(\rho,\delta)/A = \frac{\varepsilon}{\rho}(\rho,\delta). \tag{17}$$

There are three variable parameters in the QMC model which need to be fitted to experimental data, the coupling constants G_σ, G_ω and G_σ. There are some other parameters in the QMC model which are not varied. The bag radius R_B is fixed to be 1 fm, while the σ meson mass, m_σ, which is not well determined experimentally, is chosen to be 700 MeV. We also set the σ meson self-interaction parameter, λ_3, to zero in nuclear matter. The self-interaction appears to be important in the non-relativistic extension of QMC for finite nuclei [85, 86] but its effect in nuclear matter is still a subject of investigation and will be reported in future work. The ω and ρ meson masses and the isoscalar and isovector nucleon magnetic moments, which appear in the spin-orbit interaction in finite nuclei [81, 83] are taken at their physical values. The role of all the parameters is well determined and constrained. If a serious discrepancy between the QMC model prediction and some new observational and/or experimental data would occur, physics missing in the model would have to be sought, instead of further variation of existing parameters which would disturb internal consistency of the model.

The relativistic QMC model has been used for the first time for NS in 2007 [77] and predicted a heavy cold NS with $M_g \sim 1.97\ M_\odot$ with a hyperonic core, three years before it was observed [16]. Recently, the model was extended to model NS at finite temperature, QMC-A [87] and formulated for use in modeling proto-neutron stars (PNSs), core-collapse supernovae (CCSN), and, potentially, remnants of binary neutron star mergers (BNSM) https://compose.obspm.fr/eos/205,https://compose.obspm.fr/eos/206). Non-relativistic extension of the QMC model was successfully used for detailed modeling of even-even finite nuclei [85, 86, 88] and superheavy isotopes [89].

There are some variants of the QMC model of dense matter in compact objects, using simplified expressions for the bag representing the nucleon, the effective mass of the nucleon and the treatment of meson fields (see e.g.. [90–99] and refs. therein). The authors of these QMC versions allow some flexibility in their parameters not permitted in the fully self-consistent Saclay-Adelaide formulation described here.

The unique concept of the QMC model has several important consequences. As shown in Ref. [80], the model offers a natural explanation for the saturation of the nuclear force. Even more importantly, the model automatically includes many-body forces in nuclear medium and there is no need to change the number of parameters when the baryonic composition of the matter changes, for example, when hyperons appear in dense matter. In other words, matter consisting only of nucleons and matter containing the full baryon octet (nucleons and hyperons) is described by the same set of parameters. All the hyperon-nucleon and hyperon-hyperon couplings are *fixed by the quark structure* and calculated within the model. We emphasize that exchange (Fock) terms are always included in the calculations and single-particle potentials of the constituents are *calculated* within the model. This is in contrast with RMF models where the Fock terms are often omitted and the single-particle potentials form a part of input data.

4. Lecture III: Heavy ion collisions and binary neutron stars mergers

In this last lecture we address the relation between dense matter in NS and HIC and discuss the impact of the multimessenger era on understanding of the NN interaction in nuclear medium, the many-body problem.

4.1 Heavy ion collisions

Starting with heavy ion collisions (HIC), there are several facilities performing experiments in the range of beam energy per nucleon between about 35 MeV to 5 TeV, at GSI, MSU, Texas A&M, RHIC and LHC and two more are being built, FAIR in GSI and NICA in Dubna. Amongst many objectives of these complex machines, properties of dense matter at the moment of a collision of heavy projectile and target (e.g. Au,Sn,Ca) are studied through detection of the reaction products.

HIC with a low and medium beam energy (below about 10 GeV/nucleon) have been long seen as the only terrestrial experiments which could provide constraints upon the EoS of dense matter. In particular, density dependence of the symmetry energy and the incompressibility at saturation density are reflected in the elliptic and transverse flows, in dependence of the projectile and target nuclide combinations and the incident beam energy. Danielewicz et al. [100] constructed the EoS of cold SNM and PNM in the range of baryon number density up to 4.6 ρ_0, using the Boltzmann-Uhlenbeck-Uehling (BUU) transport model. The EoS was consistent with experimental data on the particle flow and in the range predicted some other models (see Fig. 21).

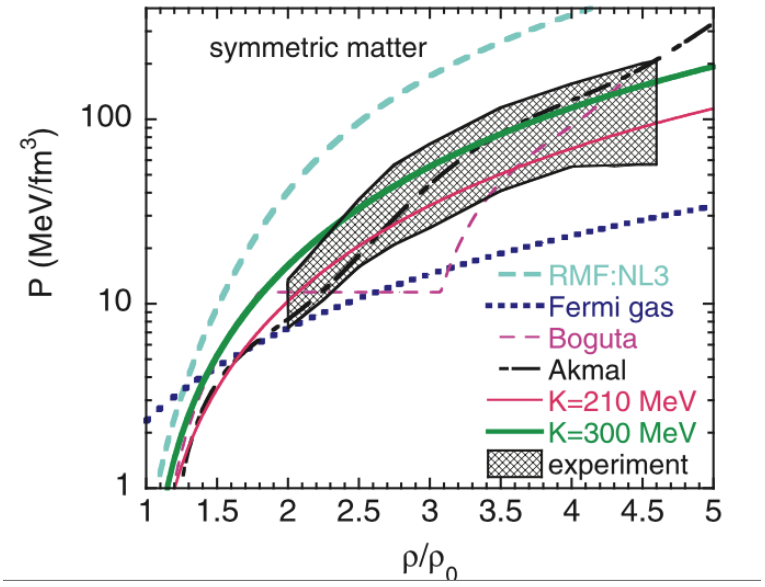

Figure 21: Zero-temperature EOS for symmetric nuclear matter as calculated in HIC transport models. The shaded region corresponds to the region of pressures consistent with the experimental flow data. The various curves and lines show predictions for different symmetric matter EOSs discussed in Ref. [100] from where the figure was adopted.

These results were revisited in 2017 (Stone, Danielewicz and Iwata [101]) who explored Ca and Sn collisions at the beam energy below 800 MeV/nucleon and concluded that the highest total particle number densities are of the order of 2.5 ρ_0, only weakly dependent on initial conditions, far lower than suggested in the original work. The maximum proton-neutron asymmetry δ was found $\sim$ 0.17 in all investigated systems and at all beam energies, scarcely above that in the colliding nuclei. This study was extended including Pb collisions as a representation of the heaviest system accesible in HIC experiments. The latest results revealed that (i) there is no increase in the

highest particle number density achieved in the collision above 2.5 to 3 ρ_0, and (ii) that there is a significant contribution of the Coulomb interaction to both the maximum total density and the isospin asymmetry at that density, which reduces the nuclear interaction induced asymmetry to below ~ 0.18 [102]. These new findings suggest that there is a serious doubt out about applicability of the HIC EoS to NS where the density in the core of heavy stars is believed to reach about 6 ρ_0 or more and the proton-neutron asymmetry is around 0.1.

However the main problem with seeking to use HIC data at low and medium beam energies to constrain the NS and CCSN EoS is that *the EoS of any system is dependent on its composition.* We compare the physical nature of matter created in the HIC and existing in cold NS cores in Table 3. The main difference stems from the duration of the collision and of the formation of a NS. The time-scale of HIC is that of the strong interaction, $\sim 10^{-24}$s. It follows that only products of the strong interaction can appear, nucleons in ground and excited states and free pions, possibly kaons. NS star develops since its birth on time scales allowing not only the strong, but most importantly, weak interactions to act, which fundamentally changes the high-density matter make-up in NS cores. The time scale of weak interaction in free space is about 10^{-13}s but can be longer in dense matter, up to $\sim$ 1 year [103, 104]. This allows appearance of weak interaction products throughout the life of a NS. Furthermore the proton-neutron asymmetry in cold NS matter is very different from that reached in HIC. Another important difference between HIC and NSs, of course, is the role of gravity in the NS, which, together with the nuclear force, determines the pressure and density distribution of the matter in the interior of the star.

Table 3: Physical properties of matter in HIC at beam energies considered in [100] and in the interior of a cold NS. No phase transitions to quark matter are included. Taken from Ref. [1].

Property	**HIC**	**NS**
Time scale	10^{-24}s	10^{-13}s
Interactions	strong	strong
		weak
Gravity	no	yes
Strangeness	conserved	not conserved in weak
Nucleons	yes	yes
Hyperons	no	yes
Pions/Kaons	yes	condensate possible
Leptons	no	yes
p/n ratio	$\sim$1	$\sim$0.1

Considering CCSN matter, it is closer to matter in HIC in one respect. The proton-neutron ratio is close to one half at the birth of the PNS. However, leptons, not present in the HIC, play an essential role in CCSN physics. Also, the existence (or not) of equilibrium in HIC, which would allow estimation of the temperature reached in the collision and its comparison with temperatures expected in CCSN events is still a subject of debate. Finally, light NS with mass around 1.4 $M_\odot$, have central density comparable with that reached in HIC. But the proton-neutron asymmetry in both systems is far from comparable.

Therefore we conclude that the HIC EoS is not applicable as a constraint for the NS EoS.

4.2 Binary NS mergers and gravitational waves

4.2.1 Observation

Observation of GW and their counterparts from BNSM has added new dimension to the search for constraints on the NS EoS. The dynamics of the BNSM has been modelled in the past to guide observation [105–109]. Since the observation, new GR based simulations have been reported, e.g. [110, 111] (for reviews see [112, 113]). Note that this subsection was mostly taken from [1].

There are three GW events involving NS reported to date. The first, GW170817 [114] is compatible with a collisison of a binary NS system with chirp mass 1.186(1) $M_\odot$, mass ratio q∈[1,1.34], and reduced tidal parameter $\tilde{\Lambda}$ ≃300 and smaller than ∼ 800. Two electromagnetic counterparts were observed, a gamma ray burst GRB170817, 1.7 s after the coalescence, and an optical signal AT2017gfo (kilonova) [115, 116], observed 0.47-18.5 days after the event.

The second, GW19025 [117] was, with 90% probability, the coalesce of two objects with masses ranging from 1.12 to 2.52 $M_\odot$ which is consistent with the individual binary components being neutron stars. Both the chirp mass and the total mass of this system are larger than any previously known binary NS system. Thus, a possibility that one or both components are light black holes cannot be ruled out from GW observation. No confirmed electromagnetic or neutrino emissions related to this event were identified.

The third, also possibly involving a NS, GW190814 [118], is compatible with a coalesce of a 22-24.3 $M_\odot$ black hole (primary) and a 2.50-2.67 $M_\odot$ compact object (secondary). No electromagnetic counterparts have been observed. This event represents a new class of binary coalescence sources with highly unequal mass and low primary spin [118]. The secondary component is either the lightest black hole or the heaviest NS ever discovered, however this is still a question of debate [119–127].

The post-merger GW signal, which is expected to have the largest luminosity and is essential for determination of the fate of the remnant, has not been observed in any of these events. It is most likely emitted at frequencies above the main sensitivity band of current detectors [128].

4.2.2 Statistical analysis in the multi-messenger era

The only observational data obtainable in detection of GW with current detectors are the amplitude change of the signal, i.e. the strain h, (a measure of its effect, specifically the ratio by which lengths are stretched or compressed, which is a dimensionless number) as shown in Fig. 22 and the electromagnetic counter parts. Fig. 22 is just a short demonstration of the challenges we face in the GW data analysis. Here, 16384 samples were taken per second and the data set was collected for 32 s, bringing 524287 data points into a database. Having collected the data, the interpretation of GW events and their counterparts crucially rely on GR models of dynamics of the mergers and assumptions on the fate and related properties of merger remnants.

The GR models based on numerical relativity simulations in 3 + 1 dimensions include physics input for the nuclear matter properties, and electromagnetic and weak interactions. However, as demonstrated in previous sections, most of this information is model dependent and not uniquely known. This is particularly true about the EoS of dense matter, independent NS measurement of gravitational mass and radius of the same object and, to certain extend, basic properties of SNM. This situation has led to the increasingly popular utilization of statistical methods based on gathering

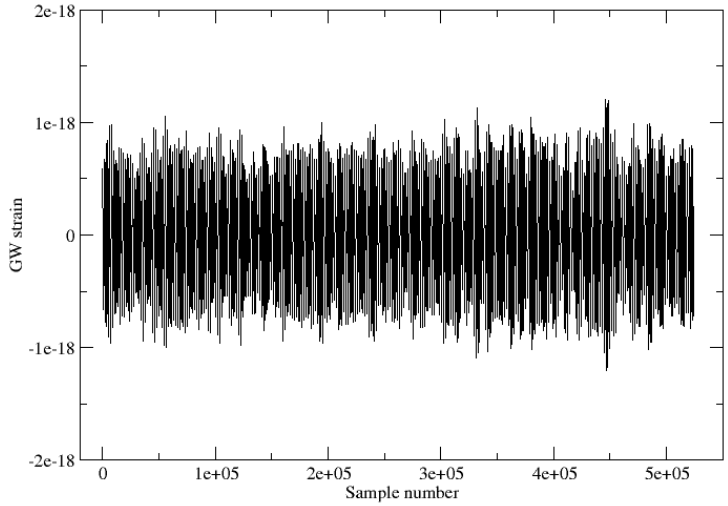

Figure 22: Gravitational wave strain for GW170817-R1 for the detector Hanford H1 (see http://losc.ligo.org). This file has 16384 samples per second starting GPS 1187008867 duration 32 s. For more information see text and https://www.gw-openscience.org/catalog/GWTC-1-confident/single/GW170817/.

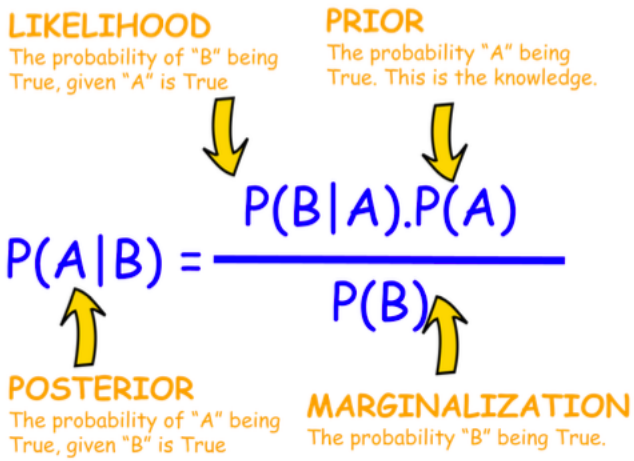

Figure 23: Definition of conditional probability based on the Bayesian theorem. Taken from https://towardsdatascience.com/bayes-rule-with-a-simple-and-practical-example-2bce3d0f4ad0.

a large number of known and hypothetical data (such as, for example, tens of of possible cold and warm EoSs) needed for construction of a prior in the Bayesian inference method (Thomas Bayes, 1763, see Fig. 23) to obtain a prediction, the posterior, for required quantities.

To make these simulations computationally viable, two major diversions from state-of-the-art NS modeling using realistic microscopic EoS are usually made. The EoS is greatly simplified to allow a minimum number of parameters to be determined by sampling, if it is approximated by piecewise polytropes, parameterized, spectral or Gaussian-type functions are used [28, 31, 38, 39, 129]. In addition, *quasi-universal* relations between selected pairs of suitably normalized NS properties are built into the simulations in the form of simple functions, e.g. polynomials, determined by only a few parameters [87, 130–136]. As demonstrated in the selected examples below, the price to pay for these simplifications and the whole statistical approach is the loss of all connection to the microscopy of NS matter. Future improved and more complete GW observations are likely to offer much enhanced sensitivity to a model content.

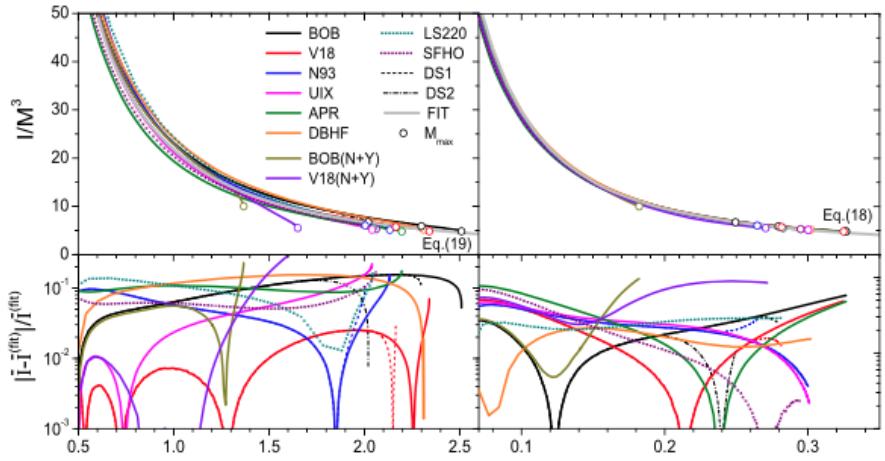

Figure 24: I/M^3 versus M (left panels) and M/R (right panels) for the 10+4 different nucleonic+hybrid EOSs listed in Ref. [134]. Configurations of M = M_{max} are indicated by markers. The grey curves show the fits according to equations (13), (16), (18), (19) in Ref. [134]. In each panel, the upper part shows the results for the different EOSs, and the lower part the fractional deviations from the grey fit curves. The figure is adopted from Ref. [134].

To illustrate the universal relations, we show in Figs. 24 and 25 the relation between the normalized moment of inertia as a function of gravitational NS mass (left panels) and the M/R ratio (right panel). The bottom panels show the deviation from polynomials (denoted by equation numbers in [134]) constructed to fit the data from 13 realistic EoS. The good quality fit puts the universal relation on a sound ground but, again, the microscopy of the EoS is lost. An interesting examination of the effect of choice of simplified EoS was reported by Miller et al. [137] who performed Bayesian inference approach which included nuclear matter variables and the inferred gravitational and baryonic masses, radii, tidal deformabilities, moments of inertia, and gravitational binding energies of neutron stars. Both the spectral and the piecewise polytropic parameterization of the EoS were used, giving similar, but not identical results. Miller et al. found that different types of measurements will play distinct roles in constraining the EOS in different density ranges. For example, better symmetry energy measurements will have a major influence somewhat below nuclear saturation density but little influence at higher densities. On the other hand, precise radius measurements or multiple tidal deformability measurements of the quality of those from GW170817

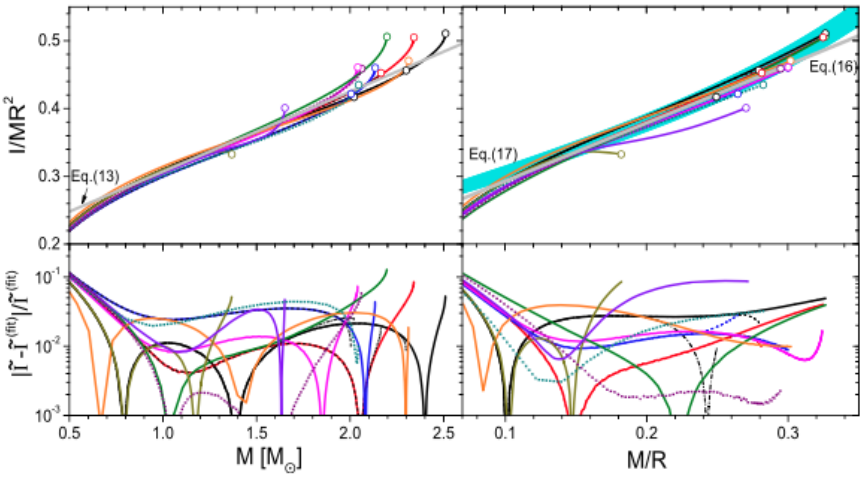

Figure 25: The same as Fig. 24 but for I/MR^2.

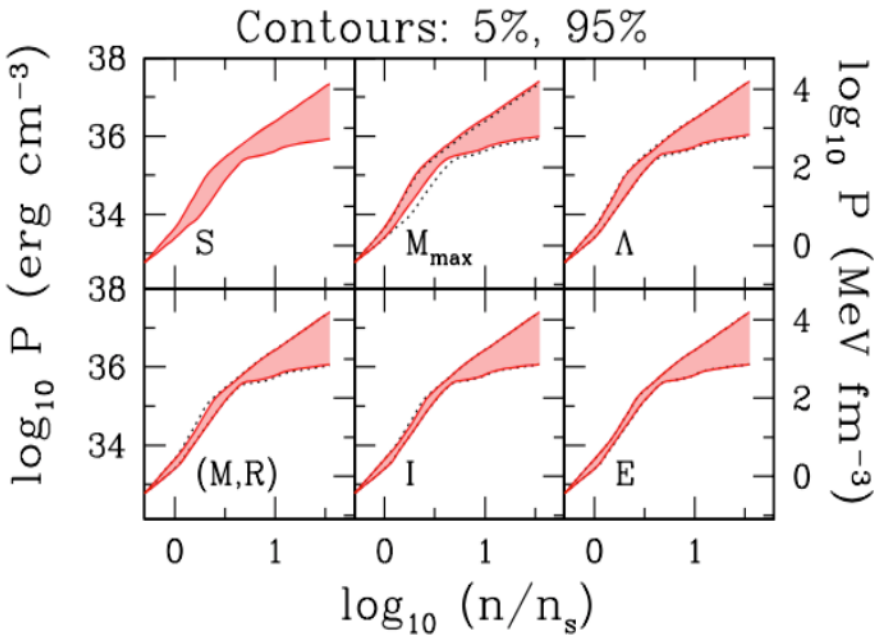

Figure 26: Various predictions of the low density EoS (below 1.5 ρ_0 as yielded by the statistical analysis by Miller et a [137] from where the figure was taken. The legend in each panel indicates which quantity was used as a constraint in the simulation: S (symmetry energy), M_{max} (maximum gravitational mass of NS), Λ tidal deformation), (M,R) hypothetical (1.4 $M_\odot$,12 km), I (moment of inertia) and E (baryonic mass). The dotted lines show the 5% and 95% quantiles for each constraint. For more explanation see text.

or better will improve our knowledge of the EOS over a broader density range.

We demonstrate these finding in Fig. 26, demonstrating constraints on the EoS constructed as a sequence of polytropes. The single quantity used as a constraint in each panel are S = 32 ± 2 MeV;

the M_{max} masses of the three most massive neutron stars; the tidal deformability Λ of GW170817; a hypothetical (M, R) = (1.4 $M_\odot$,12 km) measurement to 5% precision; a hypothetical measurement of the moment of inertia I of a 1.338 M $M_\odot$ star to 10% precision; and hypothetical knowledge of the baryonic rest mass E of a star to 0.005 M $M_\odot$ precision. There are two things to notice. These constraints apply only on NSs with central density up to 1.5 ρ_0 and are still two large to single out the most probable NS EoS even in this density region although the constraints are already at the cutting edge of the current observational techniques.

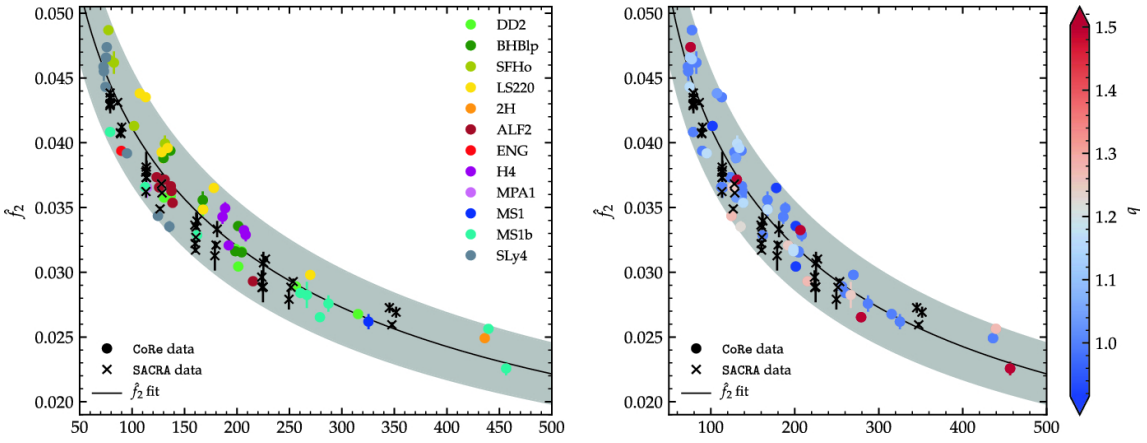

Figure 27: Phenomenological EOS-insensitive relation between the predicted GW's main peak post-merger mass scaled frequency $\hat{f}_2$ = M f_2 (y-axis) and the (modified) tidal parameter $\xi(\kappa_2^T, \nu)$ (x-axis). Both panels show the same data. The round markers correspond to the simulations of the CoRe database. For those data the EOS variation is highlighted in colors in the left panel and the mass ratio variation in the right panel. The crosses correspond to the SACRA database that also refer to a large variation of EOS (although not highlighted in the graphics). The fit is performed only on the CoRe data and the grey band represents the 90% confidence region. The caption and the figure were taken from Ref. [112] where more explanation and references can be found.

All the currently available GW signals are coming from the pre-merger stage, as post-merger signals are not yet accessible. Therefore, it seems that only cold low-mass NS and the merger dynamics can be studied in more detail, subject to assumptions on the fate of the remnant. Some models indicate that there is an approximate correlation between the predicted characteristic post-merger GW frequencies with properties of the binary and the non-rotating equilibria of NS (see e.g. [138]), with the tidal deformability playing the most important role. As shown in Fig. 27, an EoS-insensitive relation between the maximum post-merger GW signal and the pre-merger tidal deformability can be constructed. Finally, It is interesting to show a very clear dependence of the GW calculated waveform, which is in the heart of the raw GW signal analysis, on the expected fate of the remnant. Representative evolution of amplitude, frequency and the real part of the (2,2) multipole of the GW strain and luminosity in three different scenarios, prompt collapse (left panel), short-lived heavy star (middle panel) and long lived star (right panel) [112, 139], calculated using selected EoSs, is illustrated In Fig. 28. Although the waveforms may change in detail in dependence on the choice of EoS and the pre-merger conditions (the data in Fig. 28 are for equal-mass NS merger), they will be essential in interpretation of the post-merger signal when available.

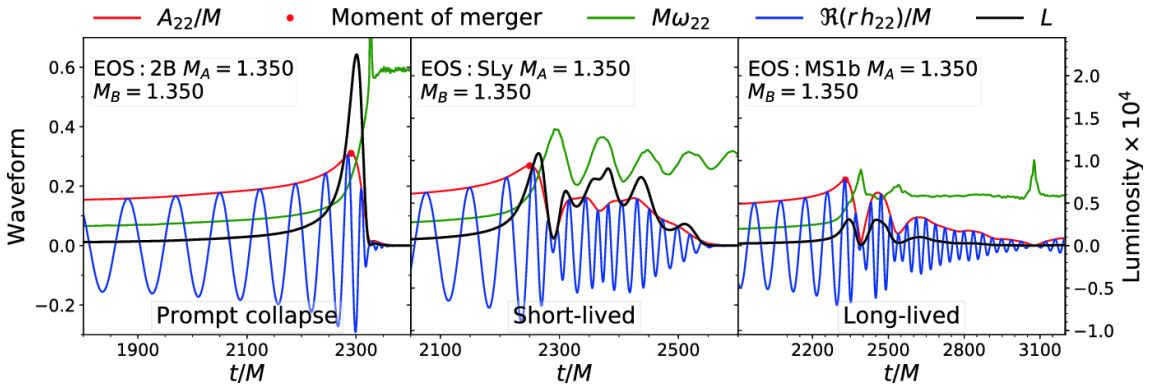

Figure 28: Gravitational waveforms for equal-mass irrotational mergers. The evolution of amplitude, frequency and real part of the (2, 2) multipole of the GW strain and luminosity are shown. From left to right: prompt collapse, short-lived, and long-lived stable remnant. Figure taken from Ref. [112].

5. Summary

In these lectures I attempted to take the audience through some aspects of the life and death of NS, from their discovery in the 1930's to their final achievement - production of GW in BNSM in the 2020's. Many details were left out, such the physics of their outer layers and the components and phase transitions in the interiors. The central focus has been on the main secret NSs have not yet disclosed to us, their EoS. Hundreds and hundreds of papers were written on this subject over the years but the final answer is not there yet. One of the reasons goes even deeper. Despite admirable effort, the microscopy of the many-body baryon-baryon interaction in medium is not understood, preventing construction of a truly realistic, unique NS EoS. The difficulty in solution of this problem led the field in recent years towards EoS-insensitive statistical methods. This is an understandable step under the circumstances. We wish to interpret data and provide guidance to future observations at least on some level. But again, increasing number of Bayesian priors is being constructed and processed in various ways, as model NS EoSs before. And the baryon-baryon interaction in medium is still waiting to be discovered.

References

[1] J.R. Stone, *Nuclear Physics and Astrophysics Constraints on the High Density Matter Equation of State*, *Universe* **7** (2021) 257.

[2] A.M. Soderberg, E. Berger, K.L. Page, P. Schady, J. Parrent, D. Pooley et al., *An extremely luminous x-ray outburst at the birth of a supernova*, *Nature* **453** (2008) 469.

[3] E. Greco, M. Miceli, S. Orlando, B. Olmi, F. Bocchino, S. Nagataki et al., *Indication of a Pulsar Wind Nebula in the Hard X-Ray Emission from SN 1987A*, *The Astrophysical Journal Letters* **908** (2021) L45.

[4] W. Baade and F. Zwicky, *Remarks on Super-Novae and Cosmic Rays*, *Physical Review* **46** (1934) 76.

[5] M. Amenomori, Y. Bao, X. Bi, D. Chen, T. Chen, W. Chen et al., *First Detection of Photons with Energy beyond 100 TeV from an Astrophysical Source*, *Physical Review Letters* **123** (2019) 051101.

[6] M. Kramer, *Millisecond Pulsars as Tools of Fundamental Physics*, *Lecture Notes Phys.* **648** (2004) 33.

[7] J.M. Cordes, M. Kramer, T.J.W. Lazio, B.W. Stappers, D.C. Backer and S. Johnston, *Pulsars as tools for fundamental physics & astrophysics*, *New Astronomy Reviews* **48** (2004) 1413.

[8] S.G. Karshenboim and E. Peik, eds., *Astrophysics, Clocks and Fundamental Constants*, Springer Berlin Heidelberg (2004), 10.1007/b13178.

[9] O. Hamil, J. Stone, M. Urbanec and G. Urbancová, *Braking index of isolated pulsars*, *Physical Review D* **91** (2015) 063007.

[10] O. Hamil, N. Stone and J. Stone, *Braking index of isolated pulsars. II. A novel two-dipole model of pulsar magnetism*, *Physical Review D* **94** (2016) 063012.

[11] M.C. Miller, F.K. Lamb, A.J. Dittmann, S. Bogdanov, Z. Arzoumanian, K.C. Gendreau et al., *The Radius of PSR J0740+6620 from NICER and XMM-Newton Data*, *The Astrophysical Journal Letters* **918** (2021) L28.

[12] G.F. Burgio, H.-J. Schulze, I. Vidaña and J.-B. Wei, *Neutron stars and the nuclear equation of state*, *Progress in Particle and Nuclear Physics* **120** (2021) 103879.

[13] J.H.Taylor, *Pulsar timing and relativistic gravity*, *Philosophical Transactions of the Royal Society of London. Series A: Physical and Engineering Sciences* **341** (1992) 117.

[14] A.G. Lyne, M. Burgay, M. Kramer, A. Possenti, R.N. Manchester, F. Camilo et al., *A Double-Pulsar System: A Rare Laboratory for Relativistic Gravity and Plasma Physics*, *Science* **303** (2004) 1153.

[15] P.C.C. Freire, C.G. Bassa, N. Wex, I.H. Stairs, D.J. Champion, S.M. Ransom et al., *On the nature and evolution of the unique binary pulsar J1903+0327*, *Monthly Notices of the Royal Astronomical Society* **412** (2011) 2763.

[16] P. Demorest, T. Pennucci, S. Ransom, M. Roberts and J. Hessels, *Shapiro Delay Measurement of A Two Solar Mass Neutron Star*, *Nature* **467** (2010) 1081 [1010.5788].

[17] E. Fonseca et al., *The NANOgrav nine-year data set: Mass and geometric measurements of binary millisecond pulsars*, *The Astrophysics Journal* **832** (2016) 167.

[18] Z. Arzoumanian et al., *The NANOGrav 11-year data set: high-precision timing of 45 millisecond pulsars*, *The Astrophysical Journal Supplement* **235** (2018) 37.

[19] J. Antoniadis et al., *A massive pulsar in a compact relativistic binary*, *Science* **340** (2013) 6131 [1304.6875].

[20] H.T. Cromartie et al., *Relativistic Shapiro delay measurements of an extremely massive millisecond pulsar*, *Nature Astronomy* **4** (2019) 72 [1904.06759].

[21] E. Fonseca, H.T. Cromartie, T.T. Pennucci, P.S. Ray, A.Y. Kirichenko, S.M. Ransom et al., *Refined mass and geometric measurements of the high-mass PSR j0740+6620*, *The Astrophysical Journal Letters* **915** (2021) L12.

[22] A.W. Steiner, J.M. Lattimer and E.F. Brown, *The neutron star mass-radius relation and the equation of state of dense matter*, *The Astrophysical Journal* **765** (2013) L5.

[23] F. Özel and P. Freire, *Masses, radii, and the equation of state of neutron stars*, *Annu. Rev. Astron. Astrophys.* **54** (2016) 401.

[24] E. Annala, T. Gorda, A. Kurkela and A. Vuorinen, *Gravitational-wave constraints on the neutron-star-matter equation of state*, *Physical Review Letters* **120** (2018) 172703.

[25] B.P. Abbott et al., *GW170817: measurements of neutron star radii and equation of state*, *Physical Review Letters* **121** (2018) 161101.

[26] G.F. Burgio, H.J. Schulze and J.B. Wei, *Nuclear physics aspects of the GW170817 neutron star merger event*, *Nucl.Part.Phys.Proc.* **306-308** (2019) 61.

[27] C.D. Capano, I. Tews, S.M. Brown, B. Margalit, S. De, S. Kumar et al., *Stringent constraints on neutron-star radii from multimessenger observations and nuclear theory*, *Nature Astronomy* **4** (2020) 625.

[28] M. Al-Mamun, A.W. Steiner, J. Nättilä, J. Lange, R. O'Shaughnessy, I. Tews et al., *Combining electromagnetic and gravitational-wave constraints on neutron-star masses and radii*, *Physical Review Letters* **126** (2021) 061101.

[29] B. Kumar and P. Landry, *Inferring neutron star properties from GW170817 with universal relations*, *Physical Review D* **99** (2019) 123026.

[30] C.A. Raithel, *Constraints on the Neutron Star Equation of State from GW170817*, *The European Physical Journal A* **55** (2019) 80 [1904.10002].

[31] R. Essick, I. Tews, P. Landry, S. Reddy and D.E. Holz, *Direct astrophysical tests of chiral effective field theory at supranuclear densities*, *Physical Review C* **102** (2020) 055803.

[32] S. De, D. Finstad, J.M. Lattimer, D.A. Brown, E. Berger and C.M. Biwer, *Tidal deformabilities and radii of neutron stars from the observation of GW170817*, *Physical Review Letters* **121** (2018) 091102.

[33] D. Radice and L. Dai, *Multimessenger parameter estimation of GW170817*, *The European Physical Journal A* **55** (2019) 50.

[34] N.B. d'Etivaux, S. Guillot, J. Margueron, N. Webb, M. Catelan and A. Reisenegger, *New constraints on the nuclear equation of state from the thermal emission of neutron stars in quiescent low-mass X-ray binaries*, *The Astrophysical Journal* **887** (2019) 48.

[35] J.-L. Jiang, S.-P. Tang, D.-S. Shao, M.-Z. Han, Y.-J. Li, Y.-Z. Wang et al., *The equation of state and some key parameters of neutron stars: Constraints from GW170817, the nuclear data, and the low-mass X-ray binary data*, *The Astrophysical Journal* **885** (2019) 39.

[36] J.-L. Jiang, S.-P. Tang, Y.-Z. Wang, Y.-Z. Fan and D.-M. Wei, *PSR J0030-0451, GW170817, and the nuclear data: joint constraints on equation of state and bulk properties of neutron stars*, *The Astrophysical Journal* **892** (2020) 55.

[37] T. Dietrich, M.W. Coughlin, P.T.H. Pang, M. Bulla, J. Heinzel, L. Issa et al., *Multimessenger constraints on the neutron-star equation of state and the Hubble constant*, *Science* **370** (2020) 1450.

[38] P. Landry and R. Essick, *Nonparametric inference of the neutron star equation of state from gravitational wave observations*, *Physical Review D* **99** (2019) 084049.

[39] P. Landry, R. Essick and K. Chatziioannou, *Nonparametric constraints on neutron star matter with existing and upcoming gravitational wave and pulsar observations*, *Physical Review D* **101** (2020) 123007.

[40] C.A. Raithel, F. Özel and D. Psaltis, *Optimized statistical approach for comparing multi-messenger neutron star data*, *The Astrophysical Journal* **908** (2021) 103.

[41] K.N. Gourgouliatos and R. Hollerbach, *Magnetic Axis Drift and Magnetic Spot Formation in Neutron Stars with Toroidal Fields*, *The Astrophysical Journal* **852** (2017) 21.

[42] A.L. Watts, N. Andersson, D. Chakrabarty, M. Feroci, K. Hebeler, G. Israel et al., *Colloquium: Measuring the neutron star equation of state using x-ray timing*, *Reviews of Modern Physics* **88** (2016) 021002.

[43] B.B. Brandt and G. Endrodi, *Qcd phase diagram with isospin chemical potential*, 2016. 10.48550/ARXIV.1611.06758.

[44] B. Brandt, G. Endrődi and S. Schmalzbauer, *QCD phase diagram for nonzero isospin-asymmetry*, *Physical Review D* **97** (2018) 054514.

[45] F. Weber, *Strange quark matter and compact stars*, *Progress in Particle and Nuclear Physics* **54** (2005) 193.

[46] N.K. Glendenning, *Compact stars: Nuclear physics, particle physics and general relativity*, Springer Science & Business Media (2012).

[47] M. Oertel, M. Hempel, T. Klähn and S. Typel, *Equations of state for supernovae and compact stars*, *Reviews of Modern Physics* **89** (2017) 015007.

[48] C.F. v. Weizsäcker, *Zur theorie der kernmassen*, *Zeitschrift fuer Physik* **96** (1935) 431.

[49] H.A. Bethe and R.F. Bacher, *Nuclear physics: a. stationary states of nuclei*, *Reviews of Modern Physics* **8** (1936) 82.

[50] H.A. Bethe, *Theory of nuclear matter*, *Annu. Revs. Nucl. Sci.* **21** (1971) 93.

[51] W.D. Myers and W.J. Switecki, *The nuclear droplet model for arbitrary shapes*, *Annals of Physics* **84** (1974) 186.

[52] P. Moller, A.J. Sierk, T. Ichikawa and H. Sagawa, *Nuclear ground-state masses and deformations: FRDM(2012)*, *Atomic Data and Nuclear Data Tables* **109-110** (2016) 1 .

[53] M.B. Tsang, J.R. Stone et al., *Constraints on the symmetry energy and neutron skins from experiments and theory*, *Physical Review C* **86** (2012) .

[54] M. Dutra, O. Lourenço, J.S. Sá Martins, A. Delfino, J.R. Stone and P.D. Stevenson, *Skyrme interaction and nuclear matter constraints*, *Physical Review C* **85** (2012) 035201 [1202.3902].

[55] M. Dutra, O. Lourenço, S.S. Avancini, B.V. Carlson, A. Delfino, D.P. Menezes et al., *Relativistic mean-field hadronic models under nuclear matter constraints*, *Physical Review C* **90** (2014) 055203 [1405.3633].

[56] C.J. Horowitz, E.F. Brown, Y. Kim, W.G. Lynch, R. Michaels, A. Ono et al., *A way forward in the study of the symmetry energy: experiment, theory, and observation*, *Journal of Physics G: Nucl. Part. Phys.* **41** (2014) 093001 [1401.5839].

[57] C. Providencia, M. Fortin, H. Pais and A. Rabhi, *Hyperonic Stars and the Nuclear Symmetry Energy*, *Frontiers in Astronomy and Space Sciences* **6** (2019) https://doi.org/10.3389/fspas.2019.00013.

[58] J.R. Stone, N.J. Stone and S.A. Moszkowski, *Incompressibility in finite nuclei and nuclear matter*, *Physical Review C* **89** (2014) 044316.

[59] M. Baldo and G.F. Burgio, *Properties of the nuclear medium*, *Reports on Progress in Physics* **75** (2012) 026301.

[60] Z.H. Li, U. Lombardo, H.-J. Schulze, W. Zuo, L.W. Chen and H.R. Ma, *Nuclear matter saturation point and symmetry energy with modern nucleon-nucleon potentials*, *Physical Review C* **74** (2006) 047504.

[61] P. Maris, J.P. Vary, S. Gandolfi, J. Carlson and S.C. Pieper, *Properties of trapped neutrons interacting with realistic nuclear Hamiltonians*, *Physical Review C* **87** (2013) 054318.

[62] A. Gezerlis, I. Tews, E. Epelbaum, S. Gandolfi, K. Hebeler, A. Nogga et al., *Quantum Monte Carlo Calculations with Chiral Effective Field Theory Interactions*, *Physical Review Letters* **111** (2013) 032501.

[63] J. Carlson, S. Gandolfi, F. Pederiva, S.C. Pieper, R. Schiavilla, K. Schmidt et al., *Quantum Monte Carlo methods for nuclear physics*, *Reviews of Modern Physics* **87** (2015) 1067.

[64] M. Piarulli, I. Bombaci, D. Logoteta, A. Lovato and R.B. Wiringa, *Benchmark calculations of pure neutron matter with realistic nucleon-nucleon interactions*, *Physical Review C* **101** (2020) 045801.

[65] S. Weinberg, *Nuclear forces from chiral lagrangians*, *Physics Letters B* **251** (1990) 288.

[66] S. Weinberg, *Three-body interactions among nucleons and pions*, *Physics Letters B* **295** (1992) 114.

[67] R. Machleidt and D.R. Entem, *Chiral effective field theory and nuclear forces*, *Physics Reports* **503** (2011) 1.

[68] D.R. Entem, R. Machleidt and Y. Nosyk, *Nucleon-nucleon scattering up to N5LO in chiral effective field theory*, *Frontiers in Physics* **8** (2020) https://doi.org/10.3389/fphy.2020.00057.

[69] C. Drischler, R. Furnstahl, J. Melendez and D. Phillips, *How well do we know the neutron-matter equation of state at the densities inside neutron stars? a Bayesian approach with correlated uncertainties*, *Physical Review Letters* **125** (2020) .

[70] C. Drischler, J.W. Holt and C. Wellenhofer, *Chiral effective field theory and the high-density nuclear equation of state*, *arXiv:2101.01709* (2021) [http://arxiv.org/abs/2101.01709v1].

[71] E. Epelbaum, "Nuclear Chiral EFT in the Precision Era." arXiv:1510.07036 PoS, 2015. 10.48550/ARXIV.1510.07036.

[72] D.R. Entem, R. Machleidt and Y. Nosyk, *High-quality two-nucleon potentials up to fifth order of the chiral expansion*, *Physical Review C* **96** (2017) 024004.

[73] J. Hoppe, C. Drischler, K. Hebeler, A. Schwenk and J. Simonis, *Probing chiral interactions up to next-to-next-to-next-to-leading order in medium-mass nuclei*, *Physical Review C* **100** (2019) 024318.

[74] C. Drischler, K. Hebeler and A. Schwenk, *Chiral interactions up to N3LO and nuclear saturation*, *Physical Review Letters* **122** (2019) 042501.

[75] T.H.R. Skyrme, *The effective nuclear potential*, *Nuclear Physics* **9** (1959) 615.

[76] D. Vautherin and D.M. Brink, *Hartree-Fock calculations with Skyrme's interaction. I. Spherical nuclei*, *Physical Reiew C* **5** (1972) 626.

[77] J.R. Stone and P.-G. Reinhard, *The Skyrme interaction in finite nuclei and nuclear matter*, *Progress in Particle and Nuclear Physics* **58** (2007) 587.

[78] E. Chabanat, E. Bonche, E. Haensel, J. Meyer and R. Schaeffer, *A Skyrme parametrization from subnuclear to neutron star densities*, *Nuclear Physics A* **627** (1997) 710.

[79] D.P. Menezes, *A Neutron Star Is Born*, *Universe* **7** (2021) 267.

[80] P.A.M. Guichon, *A possible quark mechanism for the saturation of nuclear matter*, *Physics Letters B* **200** (1988) 235.

[81] P.A.M. Guichon, K. Saito, E.N. Rodionov and A.W. Thomas, *The role of nucleon structure in finite nuclei*, *Nuclear Physics A* **601** (1996) 349 [nucl-th/9509034].

[82] P.A.M. Guichon and A.W. Thomas, *Quark structure and nuclear effective forces*, *Phys.Rev.Lett.* **93** (2004) 132502 [nucl-th/0402064].

[83] P.A.M. Guichon, J.R. Stone and A.W. Thomas, *Quark–Meson-Coupling (QMC) model for finite nuclei, nuclear matter and beyond*, *Progress in Particle and Nuclear Physics* **100** (2018) 262 [1802.08368].

[84] J. Rikovska-Stone, P.A.M. Guichon, H.H. Matevosyan and A.W. Thomas, *Cold uniform matter and neutron stars in the quark-mesons-coupling model*, *Nuclear Physics A* **792** (2007) 341 [nucl-th/0611030].

[85] K.L. Martinez, A.W. Thomas, J.R. Stone and P.A.M. Guichon, *Parameter optimization for the latest quark-meson coupling energy-density functional*, *Physical Review C* **100** (2019) 024333.

[86] K.L. Martinez, A.W. Thomas, P.A.M. Guichon and J.R. Stone, *Tensor and pairing interactions within the quark-meson coupling energy-density functional*, *Physical Review C* **102** (2020) 034304.

[87] J.R. Stone, V. Dexheimer, P.A.M. Guichon, A.W. Thomas and S. Typel, *Equation of state of hot dense hyperonic matter in the quark-meson-coupling (QMC-a) model*, *MNRAS* **502** (2021) 3476.

[88] J.R. Stone, P.A.M. Guichon, P.G. Reinhard and A.W. Thomas, *Finite nuclei in the quark-meson coupling model*, *Physical Review Letters* **116** (2016) 092501 [1601.08131].

[89] J.R. Stone, K. Morita, P.A.M. Guichon and A.W. Thomas, *Physics of even-even superheavy nuclei with $96 < z < 110$ in the quark-meson-coupling model*, *Physical Review C* **100** (2019) 044302.

[90] P.K. Panda, D.P. Menezes and C. Providência, *Hybrid stars in the quark-meson coupling model with superconducting quark matter*, *Physical Review C* **69** (2004) 025207.

[91] P.K. Panda, D.P. Menezes and C. Providência, *Stellar matter in the quark-meson-coupling model with neutrino trapping*, *Physical Review C* **69** (2004) 058801.

[92] D.P. Menezes, P.K. Panda and C. Providência, *Kaon condensation in the quark-meson coupling model and compact stars*, *Physical Review C* **72** (2005) 035802.

[93] P.K. Panda, C. Providência and D.P. Menezes, *Warm stellar matter within the quark-meson-coupling model*, *Physical Review C* **82** (2010) 045801.

[94] P.K. Panda, A.M.S. Santos, D.P. Menezes and C. Providência, *Compact stars within a soft symmetry energy quark-meson-coupling model*, *Physical Review C* **85** (2012) 055802.

[95] T. Miyatsu, T. Katayama and K. Saito, *Effects of Fock term, tensor coupling and baryon structure variation on a neutron star*, *Phys. Lett.* **B709** (2012) 242 [1110.3868].

[96] T. Miyatsu, S. Yamamuro and K. Nakazato, *A new equation of state for neutron star matter with nuclei in the crust and hyperons in the core*, *Astrophysics J.* **777** (2013) 4 [1308.6121].

[97] P.K. Panda, D.P. Menezes and C. Providência, *Effects of the symmetry energy on the kaon condensates in the quark-meson coupling model*, *Physical Review C* **89** (2014) 045803.

[98] H. Bohr, S.A. Moszkowski, P.K. Panda, C. Providência and J. da Providência, *QMC approach based on the Bogoliubov independent quark model of the nucleon*, *Int. J. Mod. Phys.* **E25** (2016) 1650007 [1512.02392].

[99] O. Lourenço, C.H. Lenzi, M. Dutra, T. Frederico, M. Bhuyan, R. Negreiros et al., *Neutron star cooling and GW170817 constraint within quark-meson coupling models.*, *Chinese Physics C* **45** (2021) 025101.

[100] P. Danielewicz, R. Lacey and W.G. Lynch, *Determination of the equation of state of dense matter*, *Science* **298** (2002) 1592.

[101] J.R. Stone, P. Danielewicz and Y. Iwata, *Proton and neutron density distributions at supranormal density in low- and medium-energy heavy-ion collisions*, *Physical Review C* **C96** (2017) 014612 [1706.01582].

[102] J.R. Stone, P. Danielewicz and Y. Iwata, *Coulomb effects in low- and medium-energy heavy-ion collisions*, *Physics Letters B* **826** (2022) 136915.

[103] P. Haensel, *Non-equilibrium neutrino emissivities and opacities of neutron star matter*, *Astronomy and Astrophysics* **262** (1992) 131.

[104] E. Gourgoulhon and p. Haensel, *Upper bounds on the neutrono burst from collapse of a neutron star into a black hole*, *Astronony and Astrophysics* **271** (1993) 187.

[105] S. Rosswog and M. Liebendörfer, *High-resolution calculations of merging neutron stars - II. Neutrino emission*, *MNRAS* **342** (2003) 673.

[106] S. Rosswog and D. Price, *MAGMA: a three-dimensional, Lagrangian magnetohydrodynamics code for merger applications*, *Monthly Notices of the Royal Astronomical Society* **379** (2007) 915.

[107] Y. Sekiguchi, K. Kiuchi, K. Kyutoku and M. Shibata, *Gravitational waves and neutrino emission from the merger of binary neutron stars*, *Physical Review Letters* **107** (2011) 051102.

[108] V. Paschalidis, Y.T. Liu, Z. Etienne and S.L. Shapiro, *Merger of binary white dwarf-neutron stars: Simulations in full general relativity*, *Physical Review D* **84** (2011) 104032.

[109] A. Endrizzi, R. Ciolfi, B. Giacomazzo, W. Kastaun and T. Kawamura, *General relativistic magnetohydrodynamic simulations of binary neutron star mergers with the APR4 equation of state*, *Classical and Quantum Gravity* **33** (2016) 164001 [http://arxiv.org/abs/1604.03445v2].

[110] D. Radice, A. Perego, F. Zappa and S. Bernuzzi, *GW170817: joint constraint on the neutron star equation of state from multimessenger observations*, *The Astrophysical Journal* **852** (2018) L29.

[111] A. Perego, S. Bernuzzi and D. Radice, *Thermodynamics conditions of matter in neutron star mergers*, *The European Physical Journal A* **55** (2019) https://doi.org/10.1140/epja/i2019.

[112] S. Bernuzzi, *Neutron star merger remnants*, *General Relativity and Gravitation* **52** (2020) 108.

[113] D. Radice, S. Bernuzzi and A. Perego, *The dynamics of binary neutron star mergers and GW170917*, *Annu.Rev.Nucl.Part.Sci.* **70** (2020) 95.

[114] B.P. Abbott et al., *GW170817: observation of gravitational waves from a binary neutron star inspiral.*, *Physical Review Letters* **119** (2017) 161101.

[115] C. Cowperthwaite P. et al., *The electromagnetic counterpart of the binary neutron star merger LIGO/Virgo GW170817. II. UV, optical, and near-infrared light curves and comparison to kilonova models*, *The Astrophysical Journal* **848** (2017) L17.

[116] M. Breschi, S. Bernuzzi, F. Zappa, M. Agathos, A. Perego, D. Radice et al., *Kilohertz gravitational waves from binary neutron star remnants: Time-domain model and constraints on extreme matter*, *Physical Review D* **100** (2019) 104029.

[117] LIGO Scientific, Virgo collaboration, *GW190814: Gravitational waves from the coalescence of a 23 solar mass black hole with a 2.6 solar mass compact object*, *Astrophysical Journal Letters* **896** (2020) L44 [2006.12611].

[118] B.P. Abbott et al., *GW190425: Observation of a compact binary coalescence with total mass ~ 3.4 M ⊙*, *The Astrophysics Journal* **892** (2020) L3.

[119] V. Dexheimer, R.O. Gomes, T. Klähn, S. Han and M. Salinas, *GW190814 as a massive rapidly-rotating neutron star with exotic degrees of freedom*, *Physical Review C* **103** (2020) 025808 [http://arxiv.org/abs/2007.08493v2].

[120] N.-B. Zhang and B.-A. Li, *GW190814 secondary component with mass 2.50 - 2.67 M⊙ as a superfast pulsar*, *The Astrophysical Journal* **902** (2020) 38.

[121] B. Biswas, R. Nandi, P. Char, S. Bose and N. Stergioulas, *GW190814: On the properties of the secondary component of the binary*, *arXiv:2010.02090* (2020) [http://arxiv.org/abs/2010.02090v1].

[122] T. Demircik, C. Ecker and M. Järvinen, *Rapidly spinning compact stars with deconfinement phase transition*, *arXiv:2009.10731v1* (2020) [http://arxiv.org/abs/2009.10731v1].

[123] Z. Roupas, *Secondary component of gravitational-wave signal GW190814 as an anisotropic neutron star*, *arXiv:2007.10679* (2020) [http://arxiv.org/abs/2007.10679v1].

[124] M. Safarzadeh and A. Loeb, *Formation of mass gap objects in highly asymmetric mergers*, *The Astrophysical Journal* **899** (2020) L15.

[125] F.J. Fattoyev, C.J. Horowitz, J. Piekarewicz and B. Reed, *GW190814: impact of a 2.6 solar mass neutron star on nucleonic equations of state*, *arXiv:2007.03799* (2020) [http://arxiv.org/abs/2007.03799v1].

[126] Y. Lim, A. Bhattacharya, J.W. Holt and D. Pati, *Revisiting constraints on the maximum neutron star mass in light of GW190814*, *arXiv:2007.06526* (2020) [http://arxiv.org/abs/2007.06526v2].

[127] D.A. Godzieba, D. Radice and S. Bernuzzi, *On the maximum mass of neutron stars and GW190814*, *The Astrophysical Journal* **908** (2021) 122.

[128] B.P. Abbott et al., *Search for post-merger gravitational waves from the remnant of the binary neutron star merger GW170817*, *The Astrophysical Journal* **851** (2017) L16.

[129] L. Lindblom, *Causal representations of neutron-star equations of state*, *Physisal Review D* **97** (2018) 123019.

[130] G. Martinon, A. Maselli, L. Gualtieri and V. Ferrari, *Rotating protoneutron stars: Spin evolution, maximum mass, and I-Love-Q relations*, *Phys. Rev. D* **90** (2014) 064026 [1406.7661].

[131] C. Breu and L. Rezzolla, *Maximum mass, moment of inertia and compactness of relativistic stars*, *MNRAS* **459** (2016) 646 [1601.06083].

[132] M. Marques, M. Oertel, M. Hempel and J. Novak, *New temperature dependent hyperonic equation of state: Application to rotating neutron star models and I-Q relations*, *Physical Review C* **96** (2017) 045806 [1706.02913].

[133] K. Yagi and N. Yunes, *Approximate universal relations for neutron stars and quark stars*, *Physics Reports* **681** (2017) 1.

[134] J.B. Wei, A. Figura, G.F. Burgio, H. Chen and H.J. Schulze, *Neutron star universal relations with microscopic equations of state*, *J.Phys. G: Nucl.Part.Phys.* **46** (2019) 034001 [1809.04315].

[135] S.S. Lenka, P. Char and S. Banik, *Properties of massive rotating protoneutron stars with hyperons: structure and universality*, *Journal of Physics. G: Nucl.Part.Phys.* **46** (2019) 105201.

[136] A.R. Raduta, M. Oertel and A. Sedrakian, *Proto-neutron stars with heavy baryons and universal relations*, *MNRAS* **499** (2020) 914.

[137] M.C. Miller, C. Chirenti and F.K. Lamb, *Constraining the Equation of State of High-density Cold Matter Using Nuclear and Astronomical Measurements*, *The Astrophysical Journal* **888** (2019) 12.

[138] A. Bauswein, N. Stergioulas and H.-T. Janka, *Revealing the high-density equation of state through binary neutron star mergers*, *Physical Review D* **90** (2014) 023002.

[139] F. Zappa, S. Bernuzzi, D. Radice, A. Perego and T. Dietrich, *Gravitational-wave luminosity of binary neutron stars mergers*, *Physical Review Letters* **120** (2018) 111101.